Physics of Fluids

RESEARCH ARTICLE | JANUARY 18 2022

Modeling of shock-induced force on an isolated particle in water and air FREE

Jacob Behrendt ; S. Balachandar ; Joshua Garno ; Thomas P. McGrath

Physics of Fluids 34, 016108 (2022)
https://doi.org/10.1063/5.0067801

Physics of Fluids ARTICLE scitation.org/journal/phf

Modeling of shock-induced force on an isolated particle in water and air

Cite as: Phys. Fluids **34**, 016108 (2022); doi: 10.1063/5.0067801
Submitted: 19 August 2021 · Accepted: 28 October 2021 ·
Published Online: 18 January 2022

View Online Export Citation CrossMark

Jacob Behrendt,[1,a)] S. Balachandar,[1,a)] Joshua Garno,[1] and Thomas P. McGrath[2]

AFFILIATIONS

[1]Department of Mechanical and Aerospace Engineering (MAE), University of Florida, Gainesville, Florida 32611, USA
[2]Naval Surface Warfare Center, Indian Head Division, Indian Head, Maryland 20640, USA

[a)]**Authors to whom correspondence should be addressed**: jbehrendt@ufl.edu and bala1s@ufl.edu

ABSTRACT

The prediction of force on an isolated particle, while a shock is passing over it, is an important problem in many natural and industrial applications. Although the flow monotonically changes from the pre-shock to the post-shock state, the particle's force has been observed to behave nonmonotonically with a sharp peak when the shock is located halfway across the particle. This nonmonotonic behavior is due to the unsteady nature of the compression and rarefaction waves that radiate as the shock diffracts around the particle and, therefore, cannot be predicted by a quasi-steady model. An accurate force model must account for the unsteady nature of the flow and the sharp discontinues in the flow properties across the shock. In this work, we test four different inviscid models and observe that the compressible Maxey–Riley–Gatignol (C-MRG) model is the most accurate based on comparison with results from particle-resolved inviscid simulations at two different Mach numbers for both water and air as the medium. The C-MRG model is first demonstrated to predict the force on a stationary particle accurately and then extended to capture the force on a moving particle. Numerical complexities regarding the implementation of the C-MRG model are also discussed.

I. INTRODUCTION

The dynamics of shock interaction with particles are key features in numerous industrial applications and natural occurrences. For example, volcanic eruptions,[1] drug delivery systems,[2] and supernovae all consist of highly compressible fluid flows with shocks and other discontinuities that propagate over a distribution of particles. In these examples, there are numerous complexities involved, such as compression and expansion waves, small-scale turbulence, and particle–particle collisions. It is crucial to quantify the physical mechanisms in these compressible multiphase interactions.

This study focuses on a fundamental problem in compressible multiphase flow: shock wave interaction with an isolated spherical particle. Our objective is to evaluate existing drag models to determine which most accurately represents the inviscid force imparted on the particle by comparison with particle-resolved simulations. The problem of shock–particle interaction, at the level of an isolated particle, has been simulated by numerous researchers and does not pose a significant computational challenge.[3–5] Particle-resolved simulations of shock propagation over hundreds of particles have been considered in recent years.[6–11] However, larger-scale compressible-flow simulations containing millions or billions of particles cannot be performed in a particle-resolved context due to the extreme number of grid points required. Instead, the simulations are performed using the Euler–Lagrange (EL) or Euler–Euler (EE) approaches, where the flow details around the individual particles are not resolved. In this context, the momentum exchange between the particles and the surrounding flow must be modeled. The force models to be evaluated in this work play a vital role in the coupling between the fluid and the particulate phases in EL and EE simulations of compressible multiphase flows and are, therefore, of great practical importance. Additionally, obtaining an accurate model of force on an isolated particle is of fundamental importance in itself since it embodies the physics of pressure (and density) waves generated by the interaction and the diffraction of the primary shock wave as it propagates around the particle.

When a planar shock propagates past an isolated stationary particle, due to the rapid change in fluid properties across the shock, the fluid state around the particle will change from the pre-shock to the high-pressure post-shock condition on the shock-interaction timescale of $\tau_{int} = d_p/U_s$, where d_p is particle diameter and U_s is the shock velocity. Though fluid pressure, density, and velocity initially vary monotonically from the pre- to post-shock state, previous experimental and simulation results[12–15] confirm the force on the particle to be nonmonotonic. In particular, the force on the particle experiences a rapid increase and reaches a peak value when the shock is roughly midway across the particle. The force then rapidly decreases and becomes negative when the shock has just moved past the particle. The force recovers to become non-negative again when the shock is well past the particle. The drag force's nonmonotonic nature, including the brief period of negative force, is driven mainly by inviscid mechanisms.

If the post-shock Mach number is subcritical (i.e., less than 0.6 in the case of a spherical particle), then the long-time inviscid force experienced by the particle after the passage of the shock decays to zero. In supercritical post-shock flow, the flow becomes supersonic at some point around the particle, introducing shocklets when the flow decelerates back to the subsonic condition. In the supersonic post-shock flow, a permanent bow-shock forms ahead of the particle. In the case of supercritical or supersonic post-shock flows, the long-time inviscid force on the particle remains nonzero, which should be correctly considered an inviscid contribution to the quasi-steady force.

The effect of viscosity on the particle force can be conceptually separated into quasi-steady and unsteady contributions.[16,17] Both these contributions become essential within a couple of shock-interaction timescales.[3] In a subcritical post-shock flow, the long-time post-shock force on the particle is dominated by the quasi-steady viscous contribution. In supercritical and supersonic flows, the long-term quasi-steady force will have viscous and inviscid contributions.

The nature of the shock–particle interaction in the three different post-shock flow regimes (subcritical, supercritical, and supersonic regimes) and the subsequent effect on particle motion, at the level of an individual particle, has been studied experimentally, numerically, and with Euler–Lagrange simulations.[12–14,18–24] These experiments and simulations focused on determining the unsteady drag a particle endures while interacting with a shock and after it has passed.

The purpose of a drag model is to determine the force on a particle in terms of the undisturbed flow seen by the particle. The term undisturbed flow refers to the flow that exists in the absence of the particle. For example, the fluid velocity U in the Stokes drag law $F = 3\pi\mu d_p U$ is the velocity of fluid that would have occupied the space of the particle, in the absence of the particle; i.e., the Stokes drag is based on the undisturbed fluid velocity at the particle. In the particle's presence, the fluid velocity in the neighborhood of the particle would be disturbed by the particle. Care must be exercised in adequately evaluating the undisturbed fluid velocity for use in the drag model in an EL or EE simulation.[25–27]

In the context of the shock–particle interaction, the undisturbed flow is well defined as the planar shock flow that approaches the particle. Nevertheless, its use in the standard drag law presents three critical challenges. First, the undisturbed flow at the particle's location rapidly varies from the pre-shock to the post-shock condition as the shock sweeps past the particle. The shock-interaction timescale τ_{int} is typically much faster than the inertial d_p/U and viscous d_p^2/ν timescales of the problem, and as a result, the particle's force cannot be treated as quasi-steady and the unsteady contributions become important. In such time-varying flows, one must use the Basset–Boussinesq–Oseen (BBO) equation to calculate the unsteady force on the particle.[28] In the context of shock–particle interaction, the compressible version of the BBO equation[29] must be used. The unsteady contributions to the drag force depend not only on the instantaneous undisturbed flow at the particle but also on the entire history of the undisturbed flow.

The second challenge is due to the abrupt transition of fluid properties across the shock, whose thickness is often much smaller than the particle diameter. As a result, the undisturbed flow that exists is the constant pre-shock (or post-shock) state before the shock arrives (or after the shock leaves). While the shock is crossing the particle, the undisturbed flow surrounding the particle is partly pre-shock and partly post-shock state. In the incompressible regime, such variation in the undisturbed flow on the scale of the particle requires the use of the Maxey–Riley–Gatignol (MRG) equation[30,31] in the particle force calculation. The MRG equation is qualitatively similar to the BBO equation, except that the undisturbed fluid properties are expressed as surface and volume averages over the particle. The compressible extension to the MRG equation derived by Parmar *et al.* and Annamalai *et al.*[32,33] is required in the context of shock–particle interaction.

The BBO and MRG force expressions have been rigorously derived and are exact in the linear zero Reynolds and Mach number limit (i.e., in the limit Re $\rightarrow 0$ and M $\rightarrow 0$). The third challenge is that the linear assumption is invalid in the case of shock–particle interaction and requires the development of nonlinear finite-Re, finite-M extension to the compressible MRG equation. Such a finite-Re, finite-M extension must necessarily be empirical. Since analytical tools are incapable of solving the nonlinear problem, empirical extensions have to be made based on experimental and particle-resolved simulation results.

The compressible MRG equation of force is an integrodifferential expression, and therefore, it is more complex than the standard quasi-steady drag expression. There have been past efforts to evaluate the importance of the various unsteady contributions to the particle force that make the MRG force expression more complex.[23,24] Various simplifying approximations have been introduced in the evaluation of the integrodifferential expression. Furthermore, there have been other efforts at modeling the net effect of the shock–particle interaction without resorting to the explicit separation of unsteady and steady contributions.[34]

There are four primary goals to the present work. (i) We will systematically consider four progressively more complex models of force on a particle and evaluate their prediction accuracy during the shock–particle interaction. The simplest model considered is the incompressible BBO (I-BBO) equation that ignores both the compressibility effect and the particle's finite size. Incompressible MRG (I-MRG) equation will then be considered to account for the finite-particle size. This will be followed by compressible BBO (C-BBO) and compressible MRG equations that account for the effect of compressibility. We will consider the nonlinear version of these models and evaluate their accuracy by comparing them against the results of particle-resolved simulations. Our attention will be focused on the inviscid forces since the modeling of quasi-steady force as a function Re and M has been well addressed.[22,35–37] (ii) We will investigate the force models in the context of both the ideal and stiffened gas equation of state (EOS). Past efforts of shock–particle interaction have generally been limited to fluids satisfying ideal gas EOS. However, many practical applications involve nonideal fluids. We consider a stiffened gas EOS with parameters consistent with liquid water. (iii) Numerical implementation of the integrodifferential expression for force requires care. Here, we will consider the numerical implementation of the different force expressions in the context of an Euler–Lagrange simulation of shock propagation over a stationary particle and evaluate the trade-off between accuracy and computation cost. The results from each model will be compared against particle-resolved simulations to determine the accuracy. (iv) Quantify the accuracy of the compressible MRG model for a moving particle. The initial discussion will assume a stationary particle, which is valid when the particle is significantly heavier than the fluid. However, in a physical experiment, the particle will be moving, and testing the performance of the model in this regime is essential.

The paper is organized as follows: Section II presents the detailed formulations of the drag force models being considered. In Sec. III, these force expressions are applied to the problem of a sharp shock front propagating over a stationary particle. The governing equations, numerical method, simulation setup, and grid resolution of particle-resolved simulations with both the ideal (air) and the stiffened (water) EOS are presented in Sec. IV. In Sec. V, we compare the different force model results with the simulation results and available experimental data. Numerical implementation of the different force models in the context of Euler–Lagrange simulations is addressed in Sec. VI. We consider the moving particle case in Sec. VII. Finally, conclusions are made in Sec. VIII.

II. FORCE MODELS

Subsections II A, II B, II C, and II D present four different force models: the incompressible BBO, incompressible MRG, compressible BBO, and compressible MRG models. The equations governing each model are presented in detail and explained, emphasizing application to the shock–particle interaction. Because this paper is concerned with early time behavior, the models are considered in the inviscid limit. These models are exact in the linear zero Reynolds and Mach number limit. Their extension to finite Reynolds and Mach number conditions is empirical.

The inviscid flow around the particle as computed in a particle-resolved simulation is far more complicated than the undisturbed flow, $\boldsymbol{u}_{un}$, which remains a simple planar shock at all times. The difference between the actual flow and the undisturbed flow is the perturbation induced by the presence of the particle. In the present case of inviscid simulations, the perturbation flow is due to the imposition of the no-penetration boundary condition at the particle's surface. Since a no-slip boundary condition is not imposed, the perturbation flow does not include the development of boundary layers. Our objective is to express the particle's inviscid force as a function of time during the early period of the shock–particle interaction in terms of the undisturbed flow.

A. Incompressible BBO (standard point-particle) model

The first model to be considered is the incompressible BBO equation,[38–40] which will also be referred to as the standard point particle model, since it is often used in Euler–Lagrange simulations of both incompressible and compressible multiphase flows. The inviscid force on a particle is expressed as the sum of three contributions:

$$\mathbf{I-BBO}: \boldsymbol{F}(t) = \underbrace{-V_p[\nabla p_{un}]_@}_{\boldsymbol{F}_{un}} + \boldsymbol{F}_{qs} + \underbrace{C_M V_p \left[\frac{\partial(\rho_{un}\boldsymbol{u}_{un})}{\partial t} + \rho_{un}\boldsymbol{u}_{un}\cdot\nabla\boldsymbol{u}_{un}\right]_@}_{\boldsymbol{F}_{iu}=\boldsymbol{F}_{iu,l}+\boldsymbol{F}_{iu,nl}}, \quad (1)$$

where $V_p = 4\pi R_p^3/3$ represents the volume of the particle. In the above, $\boldsymbol{u}_{un}$, p_{un}, and ρ_{un} correspond to the undisturbed velocity, pressure, and density. Here, the particle is taken to be stationary. The added-mass coefficient C_M is in general a function of the flow Mach number seen by the particle, and it takes a value of 1/2 in the low Mach number limit.

The first term on the right is the undisturbed flow force, meaning that this force exists even when the particle does not perturb the flow, and it acts on the spherical volume occupied by the particle. Since the undisturbed shock is taken to be inviscid, $\boldsymbol{F}_{un}$ depends only on the local pressure gradient and, therefore, often referred to as the pressure-gradient force. In the BBO formulation, the particle is taken to be much smaller than the flow scales, and the pressure gradient for the force calculation is evaluated at the center of the particle, which is represented by the notation $[\cdot]_@$. In contrast, the other two force contributions are due to the inviscid perturbation flow induced by the particle's presence. The second term on the right is the inviscid quasi-steady force, which is identically zero when the post-shock flow is subcritical. When the flow is supercritical or supersonic, it increases monotonically as the shock goes over the particle and reaches a constant value after the shock has passed.

The final term on the right is the added-mass force due to the undisturbed ambient flow's acceleration. This force will be referred to as the inviscid unsteady force, as indicated by the subscript "*iu*." In the incompressible limit, this force depends only on the instantaneous acceleration of the surrounding fluid, represented by the term within the square parenthesis, again with the subscript @ to denote that this quantity is evaluated at the center of the particle. This instantaneous relation between force and acceleration gives rise to the added-mass concept. As will be seen below, this instantaneous relationship is lost in the compressible regime, and therefore, we refer to this force by the more general term, the inviscid unsteady force. The first term within the square parenthesis is the linear form of the added-mass force that Bassett, Boussinesq, and Oseen rigorously derived.[38–40] Though the original derivation was for constant fluid density, its application in the present context is for variable density compressible flow. Therefore, the undisturbed flow density has been taken inside the derivative. Since the particle has been taken to be stationary, the time derivative following the particle d/dt has been replaced with $\partial/\partial t$. The second term within the square parenthesis is an empirical addition that accounts for the nonlinear effect of convective acceleration of the undisturbed ambient flow. This term's origin has been brilliantly articulated by Taylor[41] in the investigation of the inviscid force on a body in converging or diverging streams of fluid. Even in a steady ambient flow, spatial variations in the undisturbed ambient flow will give rise to spatial variation in impulse and an attendant added-mass force, represented by $\boldsymbol{F}_{iu,nl}$. In the limit of constant density, the two terms within the square parenthesis combine to yield the familiar added-mass force due to fluid acceleration, namely, $C_M V_p \rho_{un} D\boldsymbol{u}_{un}/Dt$, where $D/Dt = \partial/\partial t + \boldsymbol{u}_{un}\cdot\nabla$ is the total derivative following the undisturbed fluid. Finally, it should be noted that fluid velocity, density, and their gradients that appear within $[\cdot]_@$ are evaluated at the particle center.

The incompressible BBO model ignores both the compressible nature of the problem and the particle's finite size compared to the shock thickness. Subsections II B, II C, and II D will consider improved force models by relaxing these restrictions.

B. Incompressible MRG model

The point-particle model of Subsection II A is ill-suited for the problem of a sharp shock propagating over a particle. The spatial derivatives of undisturbed flow quantities (i.e., ∇p_{un} and $\nabla \boldsymbol{u}_{un}$) become singular at the shock front. For example, ∇p_{un} is identically zero on either side of the shock front and becomes infinite at the shock. However, this difficulty is avoided in an EL simulation since the numerical shock is of finite thickness and extends over a few grid points. As a result, the undisturbed flow's spatial gradients, though remain finite in an EL simulation, can become large. In fact, in an EL simulation, the I-BBO model's application will face the nonconvergence problem, since as the grid is refined, the gradients at the shock will continue to increase, leading to ever-increasing pressure-gradient and inviscid-unsteady forces.[42]

In this subsection, we consider the Faxén form of the force expression given by the MRG formulation.[30] The inviscid force on the particle is expressed as the sum of three contributions

$$\mathbf{I-MRG}: \boldsymbol{F}(t) = \underbrace{-S_p\,\overline{p_{un}\boldsymbol{n}}^S}_{\boldsymbol{F}_{un}} + \boldsymbol{F}_{qs} + \underbrace{C_M V_p \left[\frac{\partial\left(\overline{\rho_{un}\boldsymbol{u}_{un}}^V\right)}{\partial t} + \overline{\rho_{un}\boldsymbol{u}_{un}}^V \cdot \nabla \overline{\boldsymbol{u}_{un}}^V\right]}_{\boldsymbol{F}_{iu}=\boldsymbol{F}_{iu,l}+\boldsymbol{F}_{iu,nl}}, \tag{2}$$

where $S_p = 4\pi R_p^2$ is the surface area of the particle and $\boldsymbol{n}$ is the outward surface normal to the particle. The volume and surface averages over the particle are represented as $\overline{(\cdot)}^V$ and $\overline{(\cdot)}^S$, respectively. In the pressure gradient force, we have used Gauss's theorem to replace $-V_p\overline{\nabla p_{un}}^V$ by the first term on the right-hand side. The Gauss theorem is particularly useful in evaluating volume averages involving spatial gradients. Since spatial gradients of quantities, such as pressure, are infinite at the shock, it is far more convenient to evaluate $\boldsymbol{F}_{un}$ as the surface average of pressure, as given in the first term.

Similarly, in the added-mass force, the volume average has regularized the two terms within the square parenthesis. In the linear term, the product $\rho_{un}\boldsymbol{u}_{un}$ evaluated at the center of the particle undergoes a singular step-change from pre- to post-shock values when the shock moves past the particle center, whereas the volume average $\overline{\rho_{un}\boldsymbol{u}_{un}}^V$ smoothly changes over time as the shock propagates over the particle. Thus, while $\partial(\rho_{un}\boldsymbol{u}_{un})/\partial t$ cannot be evaluated in (1), the time derivative $\partial(\overline{\rho_{un}\boldsymbol{u}_{un}}^V)/\partial t$ can be precisely evaluated even in a shock flow. Similarly, in the nonlinear term, while $[\nabla \boldsymbol{u}_{un}]_@$ becomes singular when the shock is located at the center of the particle, the corresponding volume averaged version $\nabla\overline{\boldsymbol{u}_{un}}^V$ is well behaved and can be evaluated. Note that $\nabla\overline{\boldsymbol{u}_{un}}^V$ must be interpreted as the spatial gradient of the volume-averaged undisturbed flow. Again, in a constant density incompressible flow, the two terms within the square parenthesis can be combined to obtain $\rho_{un}\bar{D}\,\overline{\boldsymbol{u}_{un}}^V/Dt$, where convective acceleration $\bar{D}/Dt = \partial/\partial t + \overline{\boldsymbol{u}_{un}}^V\cdot\nabla$ is defined in terms of the volume-averaged undisturbed flow. In this manner, the Faxén form is better suited for flows with sharp gradients. There are numerous options for modeling the quasi-steady force. The quasi-steady force is modeled the same way for all force formulations and is presented later in Sec. III.

C. Compressible BBO equation

Now we consider the compressible BBO equation, which accurately accounts for the effects of compression and rarefaction waves generated as the shock propagates over the particle. The detailed derivation of the compressible BBO equation was presented in Refs. 29 and 33, and the resulting force expression for the present case of a stationary particle is

$$\mathbf{C-BBO}: \boldsymbol{F}(t) = \underbrace{-V_p[\nabla p_{un}]_@}_{\boldsymbol{F}_{un}} + \boldsymbol{F}_{qs} + \underbrace{V_p\int_{-\infty}^{t} K_{iu}\left[\frac{\partial(\rho_{un}\boldsymbol{u}_{un})}{\partial t} + \rho_{un}\boldsymbol{u}_{un}\cdot\nabla\boldsymbol{u}_{un}\right]_{@\xi} d\xi}_{\boldsymbol{F}_{iu}=\boldsymbol{F}_{iu,l}+\boldsymbol{F}_{iu,nl}}. \tag{3}$$

The main difference between the above and the incompressible version given in (1) as the standard point-particle model is that the added-mass force (the two terms within the square parenthesis) has been generalized to the inviscid unsteady force and is represented as a convolution integral. Note that the inviscid unsteady force at time t depends on the history of density-weighted acceleration of the undisturbed fluid, unlike in the incompressible limit where it is dependent only on density-weighted acceleration at the same time instant t. Since the BBO formulation ignores any spatial variation in the undisturbed flow, all undisturbed flow quantities seen by the particle are taken to be evaluated at the particle center. The notation $[\cdot]_{@\xi}$ denotes that the argument is evaluated at the center of the particle at the time ξ. The inviscid kernel is a function of time separation $t-\xi$ and also depends on the flow Mach number as seen by the particle. In the zero Mach number limit, the inviscid kernel has been analytically obtained to take the following form:[29,43,44]

$$K_{iu}(t-\xi; \mathrm{M}\to 0) = \frac{[c]_{@\xi}}{R_p}\exp\left(\frac{(t-\xi)[c]_{@\xi}}{R_p}\right)\cos\left(\frac{(t-\xi)[c]_{@\xi}}{R_p}\right), \tag{4}$$

where c is the speed of sound and R_p is the particle radius.[43,44] offered an interpretation of the above decaying oscillatory kernel in the context of a more straightforward problem of a spherical particle subjected to a quiescent ambient impulsively sent into uniform motion. In this simpler model problem, the undisturbed flow seen by the particle remains spatially uniform but instantly changes from a quiescent state to a steady nonzero uniform flow. Thus, the undisturbed flow remains spatially uniform at all times, unlike the shock problem where the flow is spatially discontinuous. In the presence of the particle, an inviscid disturbance front of radius $R_p + ct = R_P(1+\tilde{t})$ propagates away from the particle immediately following the change in the ambient flow.[29,43] Initially, the disturbance field is compressional (or expansional) upstream (or downstream) of the particle, contributing to a strong inviscid unsteady force directed along with the ambient flow. As the inviscid disturbance front propagates out, an alternating sequence of compression and expansion waves radiate out on the acoustic timescale, whose strength rapidly decays. This contributes to both the oscillatory behavior and the exponential decay of the force from the instant change.

The convolution integral can then be interpreted as follows: The density-weighted acceleration of the ambient flow at time ξ is given by the term within the square parenthesis in (3) and it contributes to inviscid unsteady force at all later times, i.e., influences force for all $t \geq \xi$. Due to causality, an acceleration at time ξ cannot cause a force at prior times, i.e., does not influence when $t < \xi$. By multiplying with the kernel K_{iu}, we properly weigh the past acceleration at ξ for its contribution to force at t. Since ambient flow acceleration seen by the particle is a function of time, the inviscid unsteady force on the particle at any time t depends on all the past acceleration history appropriately weighted by the kernel, as represented by the convolution integral.

The compressible BBO equation was originally derived in Ref. 29 by solving the linearized compressible Navier–Stokes equations for a temporally varying spatially uniform undisturbed ambient flow past a spherical particle. The linear assumption of small perturbation amplitude is strictly applicable only in the limit of an infinitesimally weak shock. The above compressible BBO equation has been modified to account for the nonlinear effects of finite-amplitude shocks. Only the first term within the square parenthesis in Eq. (3) was rigorously derived, and it represents the linear contribution $\boldsymbol{F}_{iu,l}$. The second term $\boldsymbol{F}_{iu,nl}$ accounts for the nonlinear effects. This term has not been rigorously derived. It is motivated by the incompressible counterpart given in (1). The theoretical derivation of C-BBO equation was in the zero Reynolds and zero Mach number limit, and as a result, the theory also does not account for variations in Mach number. In contrast, in the present inviscid application, the flow Mach number changes substantially across the shock. As will be discussed later, we partly address this with a Mach number-dependent kernel.

The inviscid unsteady force (3) differs from the linear compressible BBO equation obtained in Ref. 29 on three accounts: (i) The time derivative includes the undisturbed fluid density within it to account for the density variation of the undisturbed ambient flow. (ii) In the definition of the inviscid kernel, the time has been nondimensionalized by the speed of sound of the fluid seen by the particle (i.e., evaluated at the particle center) at the moment of acceleration. This is in contrast to the original derivation, where the speed of sound remained a constant at all times. (iii) The inviscid unsteady force includes the contribution $\boldsymbol{F}_{iu,nl}$ from convective acceleration.

D. Compressible MRG equation

While the standard point-particle model ($\boldsymbol{F}_{I-BBO}$) is the simplest, it could account for neither the spatial variation in the undisturbed flow nor the historical effect of the radiating acoustic waves. In the Faxén form ($\boldsymbol{F}_{I-MRG}$), we accounted for spatial variation by evaluating the undisturbed flow quantities as surface or volume averages. On the other hand, in the compressible BBO equation for $\boldsymbol{F}_{C-BBO}$, the convolution integral accounts for the history effect. As a result, the added-mass force became the inviscid unsteady force represented by the convolution integral. The compressible MRG equation is the complete model that accounts for both these effects.

For this work, the compressible MRG equation's detailed derivation is omitted; interested readers may find it in Ref. 33. Their analysis was built upon the well-known solution of a time-harmonic traveling plane wave of a given frequency propagating in a compressible fluid over a spherical particle. They solved the linearized compressible Navier–Stokes equations in the frequency domain. The force obtained in the Laplace space for a given frequency and wave number is then generalized to any arbitrary incoming flow. This was achieved by relating the radial and tangential velocity components in the Laplace space to the time-dependent surface-averaged radial velocity and volume-averaged velocity vectors. Parmar *et al.*[32] also derived the compressible version of the MRG equation, but using the reciprocal theorem instead of the fundamental solutions of plane acoustic wave scattering by a spherical particle. The total inviscid force on the particle can be written as

$$\mathbf{C-MRG}:\quad \boldsymbol{F}(t) = \underbrace{-S_p\,\overline{p_{un}\boldsymbol{n}}^S}_{\boldsymbol{F}_{un}} + \boldsymbol{F}_{qs} + \underbrace{3V_p\int_{-\infty}^{t} K_{iu}\left[\frac{\partial\,\overline{(\rho_{un}\boldsymbol{u}_{un,r})}^S}{\partial t} + \overline{\rho_{un}\boldsymbol{u}_{un}}^V\cdot\nabla\overline{\boldsymbol{u}_{un,r}}^S\right]_{\xi} d\xi}_{\boldsymbol{F}_{iu}=\boldsymbol{F}_{iu,l}+\boldsymbol{F}_{iu,nl}}, \tag{5}$$

which combines the convolution integral of the compressible BBO equation and the volume/surface averages of the Faxén form. In the above equation, the subscript "r" corresponds to the radial component of velocity and, therefore, on the surface of the particle $\boldsymbol{u}_{un,r} = (\boldsymbol{u}_{un}\cdot\boldsymbol{n})\boldsymbol{n}$, where $\boldsymbol{n}$ is the unit surface normal vector.

The interpretations of the first two terms on the right-hand side as the pressure gradient and the inviscid quasi-steady force have already been discussed. The third term is the inviscid unsteady force and has been written in the most compact form. The inviscid unsteady kernel is the same as that given in (4), and it is a function of the time separation $t-\xi$. In the limit when the ambient flow is spatially uniform around the particle, this term becomes the same as that given in the compressible BBO equation. The different forms of the kernel have been derived assuming small perturbations in the Mach number. To see this equivalence, we will use the following identity:[33]

$$\overline{\boldsymbol{w}_r}^S = \overline{(\boldsymbol{w}\cdot\boldsymbol{n})\boldsymbol{n}}^S = \frac{1}{3}\bar{\boldsymbol{w}}^V + \frac{1}{3}\overline{\boldsymbol{r}\nabla\cdot\boldsymbol{w}}^V, \tag{6}$$

where $\boldsymbol{r}$ is the radial vector from the center of the sphere. The above identity relates the surface average of the radial component of a vector $\boldsymbol{w}$ to its volume average. The identity can be used to rewrite the inviscid unsteady force as

$$\boldsymbol{F}_{iu} = \underbrace{V_p\int_{-\infty}^{t} K_{iu}\left[\frac{\partial\,\overline{(\rho_{un}\boldsymbol{u}_{un})}^V + \overline{\boldsymbol{r}\nabla\cdot(\rho_{un}\boldsymbol{u}_{un})}^V}{\partial t} + \overline{\rho_{un}\boldsymbol{u}_{un}}^V\cdot\nabla(\overline{\boldsymbol{u}_{un}}^V + \overline{\boldsymbol{r}\nabla\cdot\boldsymbol{u}_{un}}^V)\right]_{\xi} d\xi}_{\boldsymbol{F}_{iu,l1}+\boldsymbol{F}_{iu,l2}+\boldsymbol{F}_{iu,nl1}+\boldsymbol{F}_{iu,nl2}}. \tag{7}$$

In the limit, when ambient flow variation on the scale of the particle is small, the second and the fourth terms, i.e., $\boldsymbol{F}_{iu,l2}$ and $\boldsymbol{F}_{iu,nl2}$, can be ignored and their values can reasonably approximate the surface and the volume averages at the center of the particle. As in the C-BBO formulation, the first two terms that are within the time derivative account for the density-weighted temporal acceleration, while the last two terms account for the effect of convective acceleration. In this sense, the above compressible MRG equation reduces to the compressible BBO equation.

Since the speed of sound varies on the scale of the particle, the inviscid kernel must be appropriately defined as

$$K_{iu}(t-\xi;\bar{M}^V\to 0)=\frac{[\bar{c}^V]_\xi}{R_p}\exp\left(-\frac{(t-\xi)[\bar{c}^V]_\xi}{R_p}\right)\times\cos\left(\frac{(t-\xi)[\bar{c}^V]_\xi}{R_p}\right), \tag{8}$$

where $[\bar{c}^V]_\xi$ is the speed of sound of the undisturbed fluid over the volume occupied by the particle at time ξ. Thus, instead of the speed of sound evaluated at the particle center, we generalize it to the volume average to accommodate the step change in the speed of sound across the shock. Again, the above functional form of the kernel is appropriate only in the zero Mach number limit.

The work of Ref. 44 shows that the inviscid kernel, although qualitatively remains similar at finite Mach numbers, quantitatively changes with the increase in flow Mach number. The zero-Mach number kernel given above is shown in Fig. 1 along with the finite-Mach number kernel for the case of a Mach 1.22 flow moving over a particle in air. It is clear that the kernel decays and remains oscillatory even at finite Mach numbers. However, with increasing Mach number, the kernel extends for a longer time. The area under the kernel corresponds to the added-mass coefficient, which in the zero-Mach case is 1/2. The added-mass coefficient is observed to increase with the increase in Mach number. Based on this observation, we define the following simple empirical expression for the finite-Mach number kernel

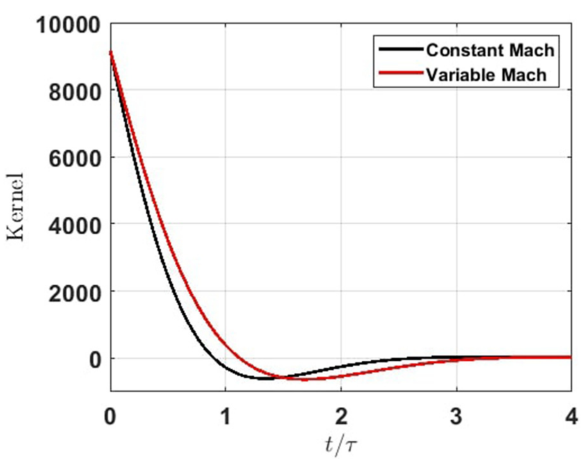

FIG. 1. Difference between constant Mach kernel (black) and variable Mach kernel (red) in air at Mach 1.22.

$$K_{iu}(t-\xi;\bar{M}^V\to 0)=\frac{[\bar{c}^V]_\xi}{R_p}\exp\left(-\alpha\frac{(t-\xi)[\bar{c}^V]_\xi}{R_p}\right)\times\cos\left(\beta\frac{(t-\xi)[\bar{c}^V]_\xi}{R_p}\right), \tag{9}$$

where the parameters α and β control the decay rate and the period of oscillation. They are functions of flow Mach number and in the limit of zero Mach number $\alpha = 1.0$ and $\beta = 1.0$. We use the finite-Mach number kernels obtained by Ref. 29 and fit the kernels with the above empirical expression to obtain the values of α and β for different flow Mach numbers in the range 0.0–0.6. An approximate fit of these parameters is given by $\alpha = -1.47\,M^2 - 0.23\,M + 1.00$ and $\beta = -1.74\,M^2 - 0.10\,M + 1.00$, where M is the Mach number. Later we will compute the inviscid unsteady force using both the zero-Mach number kernel as well as the above finite-Mach number kernel.

III. SHOCK–PARTICLE INTERACTION: FORCE MODELS

In this section, the force models described previously are specialized for interaction with a planar shock. Methods for computing the undisturbed flow force, inviscid quasi-steady force, and inviscid unsteady force are presented. As discussed previously, the incompressible and compressible BBO force expressions [i.e., Eqs. (1) and (3)] cannot be applied due to the singular nature of the spatial derivatives at the shock front. Therefore, this section concentrates on the incompressible and compressible MRG force expressions. The pre- and post-shock states, defined by the Rankine–Hugoniot equations, are formulated in the context of a stiffened gas EOS, which also encompasses an ideal gas EOS under the correct parameterization.

Figure 2 shows the undisturbed planar shock to be located at a distance x_s from the origin, where the particle's center is at the origin. The state of the stationary ambient fluid ahead of the shock (to the right of the shock) is denoted by 1, and the post-shock state on the left is denoted by 2. The density, velocity, pressure, internal energy, temperature, and speed of sound in the pre- and post-shock states of the moving planar shock are

$$(\rho,u,p,e,T,c)=\begin{cases}(\rho_2,u_2,p_2,e_2,T_2,c_2) & \text{if} \quad x<x_s,\\ (\rho_1,0,p_1,e_1,T_1,c_1) & \text{if} \quad x>x_s.\end{cases} \tag{10}$$

The particle radius R_p and the pre-shock speed of sound c_1 are taken to be the characteristic length and velocity scales. The pre-shock gas density ρ_1 and specific heat at constant pressure C_p are employed as reference scales. The characteristic time and pressure scales are then R_p/c_1 and $\rho_1 c_1^2$. The fluid is taken to obey the stiffened-gas equation of state

$$p=(\gamma-1)\rho\, e-\gamma\, p_\infty. \tag{11}$$

In the analysis that follows, we will consider parameterizations of this EOS that represent both air and water. For water, the constant $p_\infty = 0.6$ Gpa with the specific heat ratio $\gamma = 4.4$ is applied. For air, $p_\infty = 0$ (recovering the ideal gas EOS) and $\gamma = 1.4$. The inviscid Euler equations govern the undisturbed fluid flow, and accordingly, the shock is represented as a step-change in fluid properties. Rankine–Hugoniot relations that connect the pre- and post-shock states are obtained for the stiffened gas EOS, presented in Table I. A tilde denotes the nondimensional quantities, and it should be noted

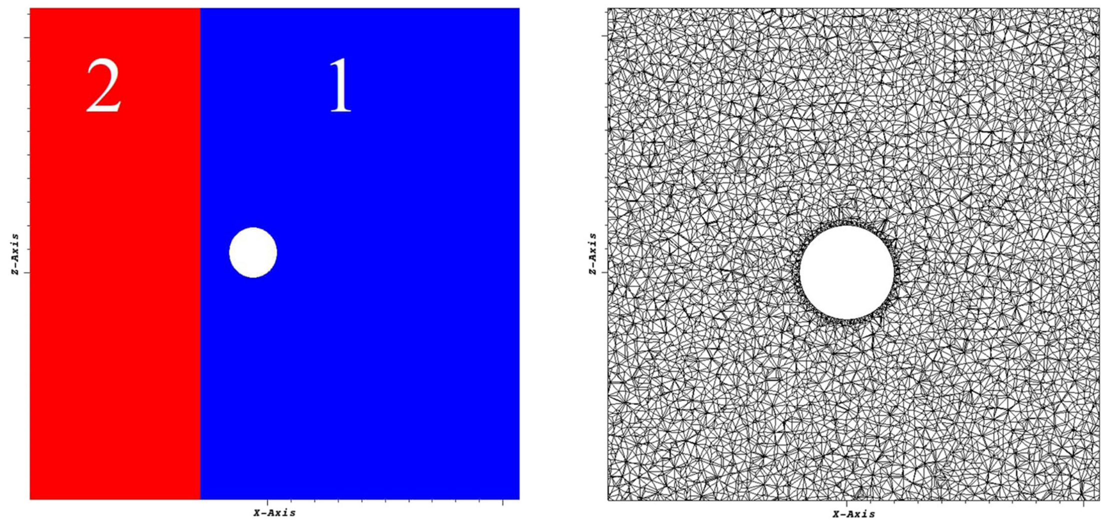

FIG. 2. The left image is the initial setup of fluid properties where Sec. II is the high-pressure region and Sec. I is the ambient fluid. The right image is a view of the body-conforming grid surrounding the particle.

that all quantities in the table are in terms of the three parameters: the specific heat ratio γ, the shock Mach number M_s, and the constant $\tilde{p}_\infty = p_\infty/(\rho_1 c_1^2)$. The corresponding results for the ideal gas EOS can be readily obtained by settling the constant $\tilde{p}_\infty = 0$.

A. Undisturbed flow force

We first address the undisturbed flow force given by the first term on the right-hand side of the compressible-MRG equation (5), which is identically the same as that predicted by the incompressible-MRG equation. Only the streamwise component of the force is nonzero and can be expressed as

$$F_{x,un}(t) = -\oint_{S_p} p_{un}(\boldsymbol{n}\cdot\boldsymbol{e}_x)\,dA = \pi\left(R_p^2 - x_s^2\right)(p_2 - p_1). \tag{12}$$

The above expression is valid only when the shock is located over the particle, i.e., only when $-R_p \le x_s \le R_p$. Otherwise, $F_{x,un} = 0$. We evaluate the surface integral by noting that part of the sphere sees the pre-shock pressure, while the rest is immersed in post-shock pressure and the factor $\pi(R_p^2 - x_s^2)$ can be recognized as the cross-sectional area of the sphere between the two pressures.

We will now nondimensionalize the force in terms of the post-shock uniform flow to define the drag coefficient. The time evolution of C_D for the undisturbed flow force becomes

I − MRG & C − MRG :

$$C_{D,un}(\tilde{t}) = \frac{F_{x,un}}{\frac{1}{2}\pi R_p^2 \rho_2 u_2^2} = \begin{cases} 2\dfrac{(1-\tilde{x}_s^2)}{\tilde{\rho}_2\tilde{u}_2^2}(\tilde{p}_2 - \tilde{p}_1) & \text{if } 0 \le \tilde{t} \le 2/M_s, \\ 0 & \text{otherwise.} \end{cases} \tag{13}$$

In the above, the nondimensional shock location is a function of time and is given by

TABLE I. Pre- and post-shock variables in nondimensional terms. Here, γ is the ratio of specific heats and M_s is the shock Mach number, which is the same as nondimensional shock speed.

Quantity	Pre-shock state (right)	Post-shock state (left)
Density	$\tilde{\rho}_1 = 1$	$\tilde{\rho}_2 = \dfrac{(\gamma+1)M_s^2}{(\gamma-1)M_s^2+2}$
Pressure	$\tilde{p}_1 = \dfrac{p_1}{\rho_1 c_1^2} = \dfrac{1}{\gamma} - \tilde{p}_\infty$	$\tilde{p}_2 = \dfrac{1}{\gamma}\left[1 + \dfrac{2\gamma}{\gamma+1}(M_s^2-1)(1+\gamma\tilde{p}_\infty)\right]$
Velocity	$\tilde{u}_1 = 0$	$\tilde{u}_2 = \dfrac{2}{\gamma+1}\left(M_s - \dfrac{1}{M_s}\right)$
Internal energy	$\tilde{e}_1 = \dfrac{e_1}{c_1^2} = \dfrac{1+\gamma(\gamma-1)\tilde{p}_\infty}{\gamma(\gamma-1)}$	$\tilde{e}_2 = \dfrac{\tilde{p}_2 + \gamma\tilde{p}_\infty}{(\gamma-1)\tilde{\rho}_2}$
Sound speed	$\tilde{c}_1 = \dfrac{\gamma(p+p_\infty)}{\rho} = 1$	$\tilde{c}_2 = \dfrac{\gamma(\tilde{p}_2+\tilde{p}_\infty)}{\tilde{\rho}_2}$

$$\tilde{x}_s = -1 + M_s \tilde{t}. \tag{14}$$

We set $\tilde{t} = t\,c_1/R_p = 0$ when the shock is located at $\tilde{x}_s = -1$, i.e., when the shock is just touching the upstream front of the particle. Also, from the above definition, at $\tilde{t} = 2/M_s$, the shock is located at the downstream end of the particle (i.e., $\tilde{x}_s = 1$). Therefore, $C_{D,un}$ is nonzero only for the limited time period $0 \le \tilde{t} \le 2/M_s$ when the shock is located over the particle. At times outside this window, when the shock is located away from the particle, $C_{D,un} = 0$.

B. Inviscid quasi-steady force

By definition, the quasi-steady force on a particle at any time t is taken to be the force that the particle would experience if the undisturbed flow seen by the particle at that time t were to remain the same in a time-independent manner. Thus, the inviscid quasi-steady force corresponds to a steady, spatially uniform undisturbed ambient flow past a stationary sphere. The inviscid quasi-steady force is identically zero when the flow around the particle is subcritical (i.e., when the flow Mach number $M < 0.6$). For $0.6 < M \le 1.0$, the flow perturbed by the particle becomes supersonic as it accelerates around the particle and results in the formation of a shocklet as the flow decelerates back to the subsonic state. When $M > 1.0$, a standing bow-shock forms ahead of the particle. The presence of a standing shocklet or a bow shock in the supercritical and supersonic flows results in a nonzero inviscid quasi-steady force on the particle. The following empirical expression for inviscid quasi-steady drag coefficient has been suggested[45]

$$C_{D,qs}(\tilde{t}) = \begin{cases} 0 & \text{if } \bar{M}^V \le 0.6, \\ 7.819 \times 10^{-9}\, e^{19.44\bar{M}^V} & \text{if } 0.6 \le \bar{M}^V \le 1.0, \\ 1 & \text{if } 1.0 \le \bar{M}^V, \end{cases} \tag{15}$$

which was obtained to fit the results of a few particle-resolved inviscid simulations of uniform ambient flow at different Mach numbers. In situations where the ambient flow spatially varies on the scale of the particle, the undisturbed flow Mach number in the above expression is taken to be the volume average as indicated by the variable $\bar{M}^V$.

In shock–particle interaction, the flow Mach number is zero ahead of the shock and M_2 behind the shock. The Mach number of the flow seen by the particle is approximated as the volume average, while the shock is located over the particle. Appendix presents expressions of volume and surface average of quantities that sharply vary over a particle. From which we obtain

$$\bar{M}^V(\tilde{t}) = \begin{cases} 0 & \text{if } \tilde{t} \le 0, \\ \left(\frac{3}{4}\tilde{x}_s - \frac{1}{4}\tilde{x}_s^3 + \frac{1}{2}\right) M_2 & \text{if } 0 \le \tilde{t} \le 2/M_s, \\ M_2 & \text{if } 2/M_s \le \tilde{t}, \end{cases} \tag{16}$$

where $\tilde{x}_s$ as a function of $\tilde{t}$ is given in (14).

C. Inviscid unsteady force

We will now evaluate the inviscid unsteady force due to shock particle interaction given in the MRG formulations. Again, we emphasize that this force cannot be calculated with the BBO formulations. Quantities, such as $V_p \partial \overline{(\rho_{un} \boldsymbol{u}_{un})}^V / \partial t$ that appear in the incompressible and compressible MRG equations, are evaluated using identities that are derived in Appendix. They are then nondimensionalized to convert them into drag coefficients. The resulting nondimensional inviscid unsteady force of the incompressible MRG model can be expressed as

$$\mathbf{I-MRG}: \quad C_{D,iu}(\tilde{t}) = \left[\tilde{I}_{l1} + \tilde{I}_{nl1}\right]_{\tilde{t}}, \tag{17}$$

where the terms on the right-hand side are evaluated at the same instance as the inviscid unsteady force. The corresponding convolution integral of the compressible MRG model becomes

$$\mathbf{C-MRG}: \quad C_{D,iu}(\tilde{t}) = \int_{\tilde{\xi}=-\infty}^{\tilde{t}} K_{\text{iu}} \left[\tilde{I}_{l1} + \tilde{I}_{l2} + \tilde{I}_{nl1} + \tilde{I}_{nl2}\right]_{\tilde{\xi}} d\tilde{\xi}, \tag{18}$$

where the integrands are evaluated for $-\infty \le \tilde{\xi} \le \tilde{t}$. The four integrand functions are evaluated using the identities of Appendix as

$$\begin{bmatrix} \tilde{I}_{l1} \\ \tilde{I}_{l2} \\ \tilde{I}_{nl1} \\ \tilde{I}_{nl2} \end{bmatrix}_{\tilde{t},\tilde{\xi}} = \begin{cases} 2\dfrac{M_s}{\tilde{u}_2}(1-\tilde{x}_s^2) \\ 2\dfrac{M_s}{\tilde{u}_2}(3\tilde{x}_s^2-1) \\ -\left(\dfrac{3}{2}\tilde{x}_s - \dfrac{1}{2}\tilde{x}_s^3 + 1\right)(1-\tilde{x}_s^2) \\ -\left(\dfrac{3}{2}\tilde{x}_s - \dfrac{1}{2}\tilde{x}_s^3 + 1\right)(3\tilde{x}_s^2-1) \end{cases} \quad \text{for } 0 \le \tilde{t}, \tilde{\xi} \le 2/M_s. \tag{19}$$

In the case of I-MRG model, $\tilde{I}_{l1}$ and $\tilde{I}_{nl1}$ are nonzero only during the interval $0 \le \tilde{t} \le 2/M_s$ when the shock is located over the particle. In the case of C-MRG model, from (14), we have $\tilde{x}_s(\tilde{\xi}) = -1 + M_s\tilde{\xi}$. The integrands are nonzero only during the time interval when the shock is located over the particle and the integrands are zero before shock arrival (i.e., $\tilde{\xi} < 0$) and after the shock has gone past the back end of the particle (i.e., $\tilde{\xi} > 2/M_s$). Now that the integrand is known explicitly, the convolution integral (18) can be carried out for any specified kernel K_{iu}. As defined in (8), K_{iu} depends on volume averaged speed of sound, which using the identities of Appendix can be expressed as

$$\bar{c}^V(\tilde{t}) = \begin{cases} c_1 & \text{if } \tilde{t} \le 0, \\ \left(\frac{3}{4}\tilde{x}_s - \frac{1}{4}\tilde{x}_s^3\right)(c_2 - c_1) + \dfrac{c_1 + c_2}{2} & \text{if } 0 \le \tilde{t} \le 2/M_s, \\ c_2 & \text{if } 2/M_s \le \tilde{t}. \end{cases} \tag{20}$$

IV. PARTICLE-RESOLVED SIMULATIONS

The above theoretical models of force prediction of shock–particle interaction will be evaluated by comparing them against inviscid particle-resolved simulations. Our focus on early time inviscid mechanisms that dominate shock–particle interaction ignores the viscous and thermal effects. An in-depth discussion on timescales can be found in Refs. 24 and 51. The acoustic timescale of the problem is d_p/c, where d_p is the particle diameter and c is the speed of sound. The viscous timescale of vorticity diffusion is d_p^2/ν, where ν is the kinematic viscosity of the fluid. The ratio of acoustic to viscous timescale goes as Ma/Re. Based on this, one may estimate the effect of viscosity to be at a much later time than the inviscid effects at $O(1)$ Mach number and $O(100)$ or more Reynolds number. However, this estimation is not entirely correct. As discussed in Mehta *et al.*,[51] vorticity starts growing on the sphere immediately following the passage of the shock and viscous effects start to become important as soon as the shock has moved a few diameters downstream of the particle.

The applicable three-dimensional equations governing inviscid fluid dynamics are given by

$$\frac{\partial \rho}{\partial t} + \nabla \cdot (\rho \mathbf{u}) = 0, \tag{21}$$

$$\frac{\partial (\rho \mathbf{u})}{\partial t} + \nabla \cdot (\rho \mathbf{u}\mathbf{u}) + \nabla p = 0, \tag{22}$$

$$\frac{\partial E}{\partial t} + \nabla \cdot ((E + p)\mathbf{u}) = 0, \tag{23}$$

where ρ is the density, $\boldsymbol{u} = (u, v, w)$ is the velocity vector, p is the pressure, and E is the total energy per unit volume calculated as

$$E = \rho\left(e + \frac{1}{2}\mathbf{u} \cdot \mathbf{u}\right), \tag{24}$$

where e is the internal energy. Inviscid simulations were performed for both air and water using the stiffened gas equation of state.

A. Numerical method

The Euler equations are solved using a finite-volume solver on a body-conforming unstructured grid. The fluid flow exterior to the sphere is discretized with a well-resolved unstructured grid. The inviscid fluxes are computed using a second-order accurate Advective Upstream Splitting Method (AUSM+) scheme.[46] The gradients are modified using a weighted essentially nonoscillatory (WENO) reconstruction technique.[47] The third-order Runga–Kutta method is used to carry out the time integration. This code has been tested and validated previously for a variety of problems involving compressible flows with shock waves.[14,23,24,48]

The particle is initially assumed to be rigid and stationary, and particle movement is discussed in Sec. VII. The assumption of a stationary particle is appropriate for a freely moving particle only when it is much heavier than the surrounding fluid. Nevertheless, the interest here is understanding force modeling in the limit of a particle held stationary. The net force on the particle is obtained by surface integration of the pressure distribution. The nonzero component of force is only along the streamwise x-direction, whose time evolution is monitored to obtain particle-resolved inviscid drag coefficient as a function of time.

The particle is placed at the center of a three-dimensional rectangular box. A slice through the center of the box with the particle is shown in Fig. 2 along with a view of the grid around the particle. The domain length in the transverse directions is 15 particle diameters, which ensures that there is no interference with reflections along the side boundaries during the simulations. The computational domain extends 7.5 and 15 particle diameters upstream and downstream of the particle along the streamwise direction. The boundaries of the computational domain in the x-direction are sufficiently far away to allow the force on the particle to reach a post-shock constant value. For the initial condition, the computational domain is split into two distinct regions: (i) shocked fluid that is upstream of the incident (primary) shock referred to as state 2 (red region) and (ii) pre-shock quiescent ambient fluid into which the incident shock will move referred to as state 1 (blue region). Once the incident shock hits the particle, it will diffract around it, while compressional waves reflect off the particle. The upstream boundary is considered a constant inflow boundary with properties equal to the post-shock flow that will sustain the shock. The downstream boundary is taken to be quiescent. Meanwhile, all other boundaries, including the particle surface, are treated as slip walls.

Two different shock Mach numbers of $M_s = 1.22$ and 3.0 are considered. The quiescent pre-shock state in water is chosen to be $p_1 = 101\,325$ Pa and $\rho_1 = 998.0$ kg/m^3, and in air, the ambient pressure is the same but $\rho_1 = 1.205$ kg/m^3. Table II gives the post-shock conditions calculated using Rankine–Hugoniot relations (see Table I) for all four cases to be considered. The naming convention for the cases begins with the fluid medium, W for water and A for air, then the shockwave speed, LM for lower Mach number and HM for higher Mach number.

B. Grid resolution

The particle-resolved three-dimensional simulations were performed using an unstructured tetrahedral grid. To generate the mesh on the sphere's surface, DistMesh[49] is used. After this step is completed, TetGen[50] is utilized to create the body-conforming unstructured tetrahedral mesh to span the computational domain. The two biggest factors that impact the solution accuracy and shock sharpness are the elements' quality and size. Also, mesh resolution on the particle must be refined to calculate the net force correctly. The aspect ratio and maximum element volume control each element's quality and size in the domain. A specified maximum allowable element size constrains the mesh resolution on the particle.

There have already been several studies that have evaluated the grid resolution requirements for inviscid shock–particle interaction. Of particular importance is the study by Ref. 51 who investigated grid resolution requirement in the context of a face-centered cubic (FCC) array of particles to determine how the element size and surface mesh resolution influenced the particle force. In summary, twenty-five different grids were tested that varied the volume and surface meshes. The optimal cell count that had the best balance between numerical error and computation cost was identified based on the information presented. Using their recommendation, we employ 3 913 694 tetrahedral elements within the domain and 14 888 elements on the particle surface. In addition, we have performed a grid independence study for

TABLE II. Values for primary shock Mach number M_s; post-shock pressure p_{ps}; post-shock density ρ_{ps}; post-shock velocity u_{ps}; post-shock Mach number $M_{ps} = u_{ps}/c_{ps}$, where c_{ps} is the post-shock speed of sound; shock velocity u_s; and $\tau = d_p/u_s$.

Case	M_s	p_2 (10^6 Pa)	ρ_2 (kg/m^3)	u_2 (m/s)	M_2	u_s (m/s)	τ (ms)
W–LM	1.22	477.73	1136.1	241.2	0.118	1984.4	0.0403
W–HM	3.0	7823.7	1487.8	1606.5	0.322	4879.7	0.0163
A–LM	1.22	0.1591	1.6582	114.47	0.312	418.63	0.1911
A–HM	3.0	1.0470	4.647 00	762.53	1.358	1029.4	0.0777

an isolated particle in water, to investigate the effect of grid resolution with varying EOS. Changing the material from air to water did not significantly impact the grid convergence results. A converged grid for air was also able to produce converged results in water.

C. Simulation flow fields

To understand the flow around the particle for both the water and air cases, nondimensional pressure and velocity magnitude contour plots for the Mach 3 cases are shown in Figs. 3 and 4. The pressure and velocity plots were normalized by the ambient pre-shock pressure and sound speed, respectively. Due to the axisymmetric nature of the problem, the pressure and velocity fields are shown only on a single plane passing through the particle center. The results are shown at two different times, immediately and sometime after the incident shock passage. In the pressure plots, outward radiation of compressional and rarefaction waves can be seen in the case of water, Figs. 3(a) and 3(b). In the velocity plots, Figs. 3(c) and 3(d), it can be seen that the flow velocity is small at the front and back stagnation points, while it increases as the flow accelerates around the particle. However, in the case of water, the flow remains subsonic everywhere. The effect of the outward radiating waves can also be observed. The results for the two other cases not shown (water and air at $M = 1.22$) are qualitatively similar to those shown in Fig. 3, where the post-shock flow in all three cases is subsonic. The case of air at $M = 3$ shown in Fig. 4 is different due to the supersonic nature of the post-shock flow. A bow shock can be seen to develop ahead of the particle since the compression, and rarefaction waves cannot propagate upstream into the supersonic post-shock flow. At the later time shown, the bow shock is nearly fully formed. The effect of the permanent bow shock on the structure of the velocity field around the particle can also be observed. The time history of the particle's net force due to the flow field is the object of modeling interest.

The resulting force for all four cases calculated from Eqs. (13), (15), and (18) is shown in Fig. 5. These figures show notable similarities and differences between the air and water cases. The similarities include a sharp rise to a peak value and a distinct peak when the shock is about halfway past the particle. The clearest difference between the two media is the peak force in water that is about 2.5 times greater than in air. With a Mach 1.22 shock, the peak drag in air is 7.49 and in water the peak value is 19.22. Note that the drag coefficient, because of its nondimensionalization, already accounts for the post-shock condition's density and velocity. Thus, the large difference in C_D between air and water highlights the EOS's importance. In the present simulations, though the shock Mach number remains the same, both p_∞ and γ are different between water and air. In essence, for the same shock Mach number, the much larger jump in pressure across the shock is responsible for the higher pressure-gradient force $\boldsymbol{F}_{un}$ and the higher speed of sound contributes to higher inviscid unsteady force $\boldsymbol{F}_{in}$. Clearly, it would be an error to use the inviscid C_D obtained for one fluid to another with a different EOS.

When looking at the air Mach 3.0 line (dashed black), it is the only one to have a nonzero drag long after the shock has passed. This is because the post-shock flow in this simulation is in the supersonic regime. A comparison between the post-shock states for water and air as a function of incident Mach number is shown in Fig. 6, where the

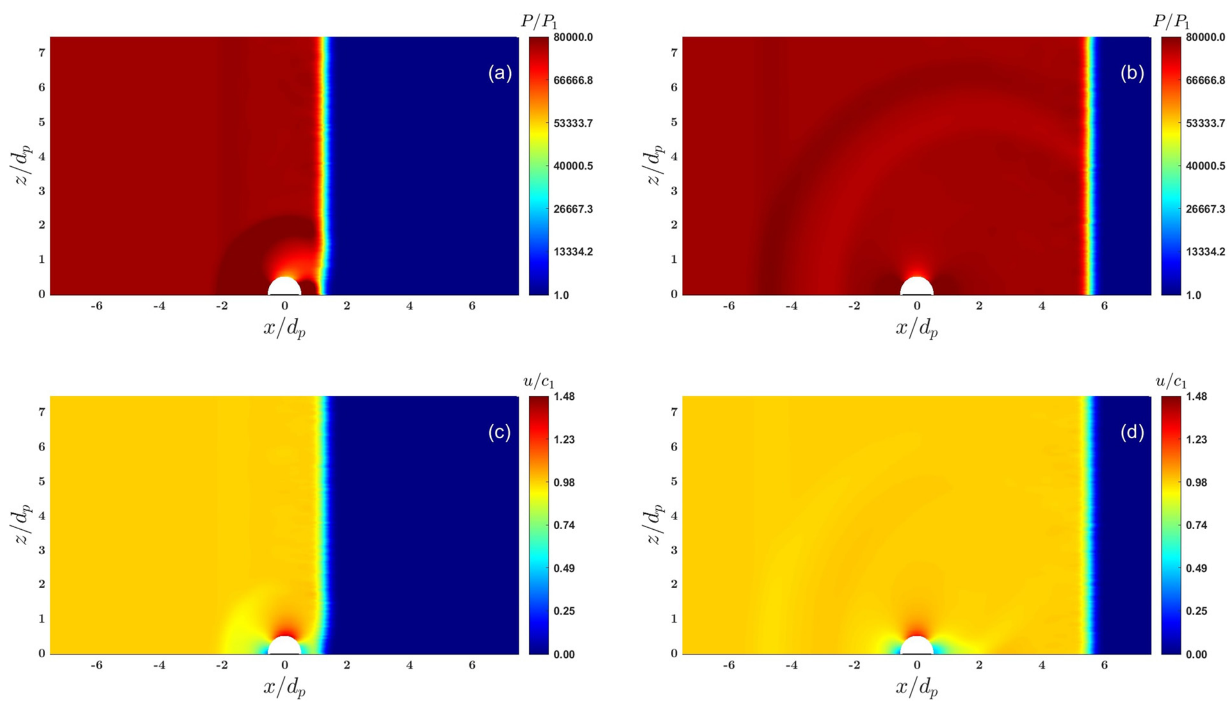

FIG. 3. (a) and (b) Contour plots of normalized pressure p/p_1 in water at $t/\tau = 2, 6$; $M_s = 3.0$, $P_1 = 101\,325$ Pa; the axes are scaled by particle diameter d_p. Frames (c) and (d) show the corresponding normalized velocity magnitude, u/c_1.

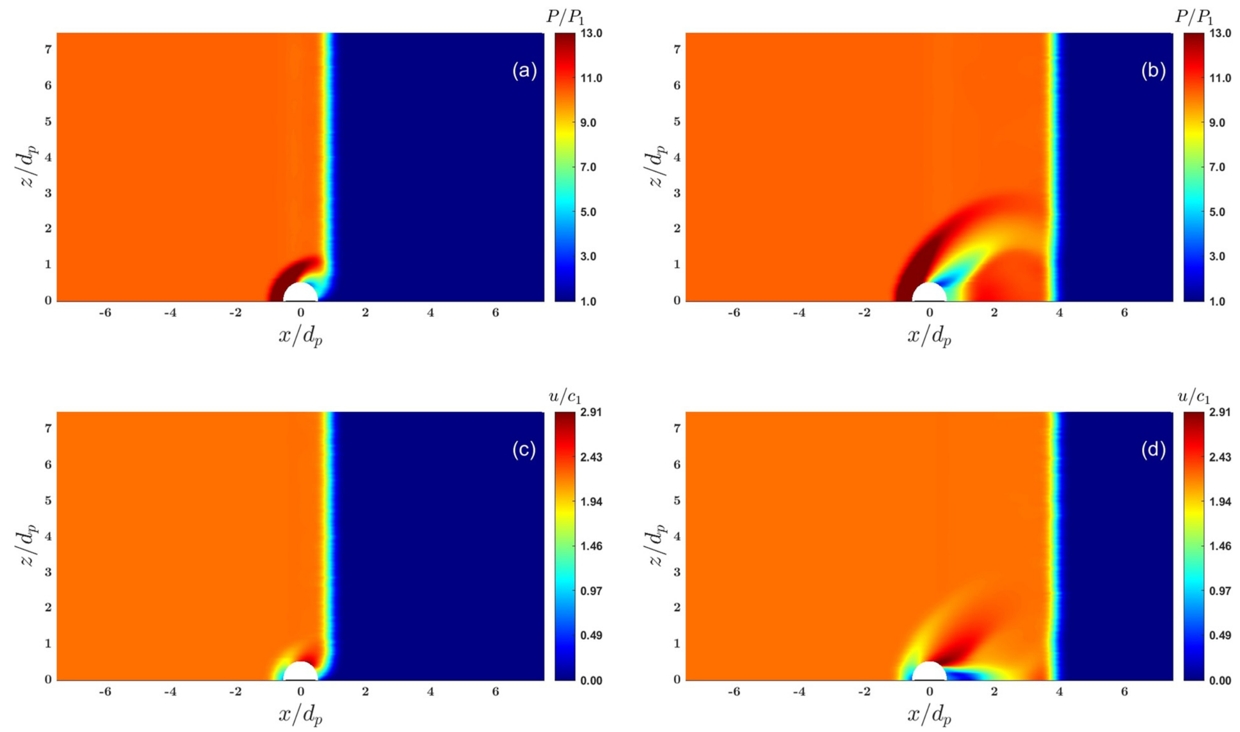

FIG. 4. (a) and (b) Contour plots of normalized pressure $u/c_1p/p_1$ in air at $t/\tau = 1.5, 4.5$; $M_s = 3.0$, $P_1 = 101\,325$ Pa; the axes are scaled by particle diameter d_p. Frames (c) and (d) show the corresponding normalized velocity magnitude, u/c_1.

stiffened gas result is the red line and ideal gas is the blue line. The horizontal dashed black lines at 0.6 and 1.0 show the cutoffs for the 3.0 post-shock regimes, subcritical, supercritical, and supersonic. If the post-shock flow is in the supercritical or supersonic regime, there will be formation of shocklets or bowshocks, causing nonzero force on the particle. The vertical dashed black lines are at the shock Mach numbers used in the simulations, 1.22 and 3.0. One can see that the ideal gas EOS goes through each of the three different areas. However, with the stiffened gas EOS and the parameters presented, it is in the subcritical regime for all Mach numbers considered. For air Mach 3.0, the post-shock flow is supersonic, leading to a nonzero force at all times after the shock has passed. The other three cases are in the subcritical range and have similar drag curves but different levels of magnitude. As stated previously, the goal is to find an accurate model that can

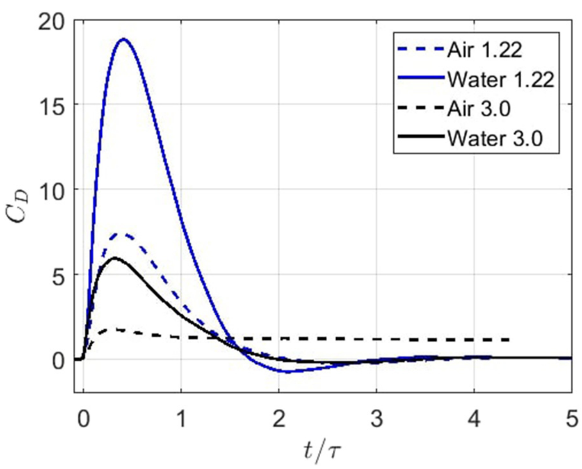

FIG. 5. C_D vs t/τ for all cases, air 1.22 (dashed blue line), water 1.22 (solid blue line), air 3.0 (dashed black line), and water 3.0 (solid black line).

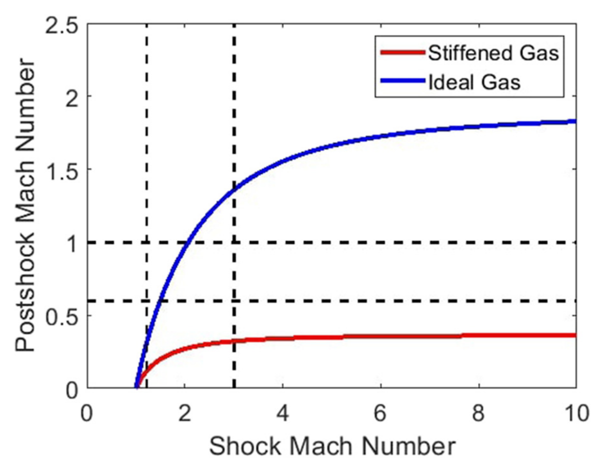

FIG. 6. Comparing the post-shock Mach numbers of stiffened gas EOS for water (red) vs the ideal gas EOS of air (blue).

predict these drag curves without performing a particle-resolved simulation.

V. MODEL PREDICTION AND PERFORMANCE

This section compares the different force models to the drag calculated from the simulations. Only the I-MRG and C-MRG models can be used because the gradients in the BBO models cannot be evaluated when studying a sharp discontinuity like a shockwave. For the MRG equations, each force component is calculated then, using superposition, the overall force prediction is computed by adding the components together. The accuracy of the models is determined by comparing the force prediction and impulse of the models to the particle resolved (PR) Direct Numerical Simulation (DNS) results.

A. I-MRG and C-MRG model predictions

In Fig. 7, the three different force components of the I-MRG model are shown for the four cases listed in Table II, where $C_{D,un}$, $C_{D,qs}$, and $C_{D,iu}$ were computed using (13), (15), and (17) with the zero Mach kernel (8). The difference between the two kernels will be evaluated later when compared to the particle-resolved results. According to (17), the inviscid unsteady force $C_{D,iu}$ can be divided into a linear contribution $C_{D,iu,l1}$ and a nonlinear contribution $C_{D,iu,nl1}$. Both of which are plotted in Fig. 7. First and foremost, all the force components are nonzero only when the particle interacts with the shock, except the quasi-steady force in the air Mach 3.0 case. This is due to the instantaneous relationship between the flow state and the particle's force, with no memory effect from the past flow states. This contrasts with experimental and particle-resolved simulation results. It is observed that the inviscid force persists after the shock has moved past the particle.

In all four cases, the ordering of the forces is as follows: $C_{D,iu,l1} > C_{D,un} > |C_{D,iu,nl1}|$, where the nonlinear portion of the inviscid unsteady force is negative (i.e., directed opposite to the flow) and its magnitude is substantially smaller than the other two. Also, while $C_{D,iu,l1}$ and $C_{D,un}$ are symmetric about $t/\tau = 1/2$ and parabolic in shape, the nonlinear contribution $C_{D,iu,nl1}$ is asymmetric and skewed toward later time when the shock is located at the back section of the particle. As a result, the total inviscid force is also asymmetric, with the peak force occurring slightly before the ambient shock arrives at the center of the particle. This asymmetry of the total force may not be readily apparent due to the small magnitude of $C_{D,iu,nl1}$. The only case

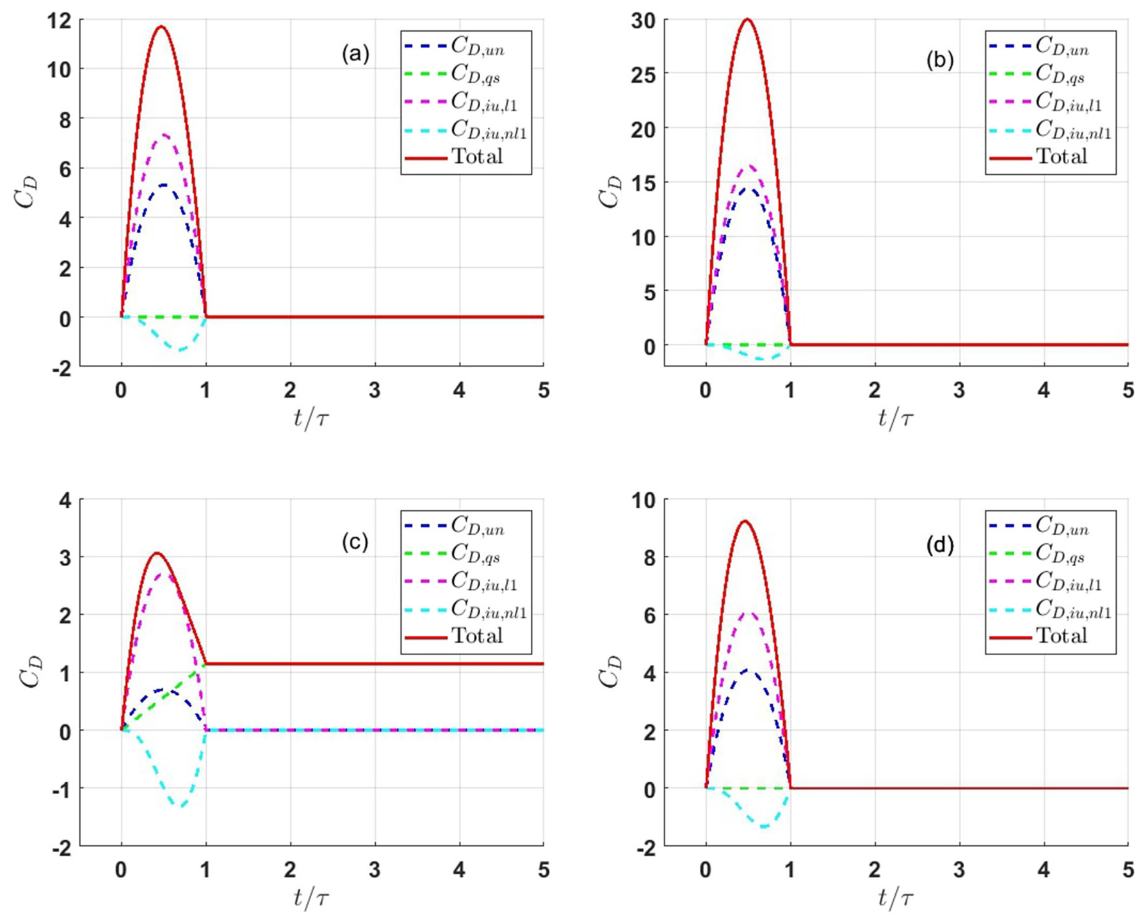

FIG. 7. Plot of each force component in I-MRG model on an isolated particle as a function of t/τ, $C_{D,un}$ (dashed blue), $C_{D,qs}$ (dashed green), $C_{D,iu,l1}$ (dashed magenta), $C_{D,iu,nl1}$ (dashed cyan), total force (solid red), (a) air 1.22, (b) water 1.22, (c) air 3.0, and (d) water 3.0.

where the quasi-steady force is nonzero is the Mach 3.0 air because of the supersonic nature of the post-shock flow. The presence of a permanent bow shock ahead of the particle (after the incoming ambient shock passage) leads to a sustained nonzero force on the particle. According to the I-MRG model, only the quasi-steady force is monotonic, while the other forces are nonmonotonic.

The results presented in Fig. 7 capture the nonmonotonic nature of the unsteady contributions to the inviscid force. However, they do not include the important effect of flow compressibility. Figure 8 presents the three contributions to the inviscid force and the total computed with the compressible MRG model. When comparing the I-MRG and C-MRG models, their differences are only the inviscid unsteady contribution, while the undisturbed flow and quasi-steady forces are identical between the two models. In the C-MRG model, the inviscid unsteady force is given by (18). Unlike in the incompressible model, the inviscid unsteady force now extends even after the shock passage, and it exhibits an oscillatory decay following the nature of K_{iu}. The effect of compressibility is that $C_{D,iu}$ depends on the past history of density-weighted acceleration. This history effect significantly changes the shape of the linear part of the inviscid unsteady force.

In the C-MRG model, $C_{D,iu,l} = C_{D,iu,l1} + C_{D,iu,l2}$ rises with the undisturbed flow force initially, but around $t = 0.25\tau$ the force reaches a local maximum and starts to decrease. The reduction continues until about $t = 0.75\tau$, after which the force again increases to reach a second maximum at $t = \tau$. Even after the shock has passed, the linear portion of the inviscid unsteady force is nonzero until about 3τ. This behavior is not seen in the I-MRG model. Finally, the nonlinear portion of the inviscid unsteady force is also different between them. The I-MRG model reaches its minimum at 0.75 τ, while the minimum in the C-MRG model is reached at 1τ and is nonzero for a period after the shock has passed. The nonlinear contribution $C_{D,iu,nl}$ is negative and increases in magnitude as the shock travels from the front to the particle's rear. Once the shock is past the particle, $C_{D,iu,nl} = C_{D,iu,nl1} + C_{D,iu,nl2}$ shows the expected oscillatory decay.

The important effects of compressibility in the total inviscid force on the particle (the red curves) can be summarized as follows: (i) The peak force in the C-MRG model is substantially lower than the I-MRG model, and this is due to the reduction in the peak value of the inviscid unsteady force; (ii) on the other hand, even without the quasi-steady contribution, the total force remains substantial after the passage of

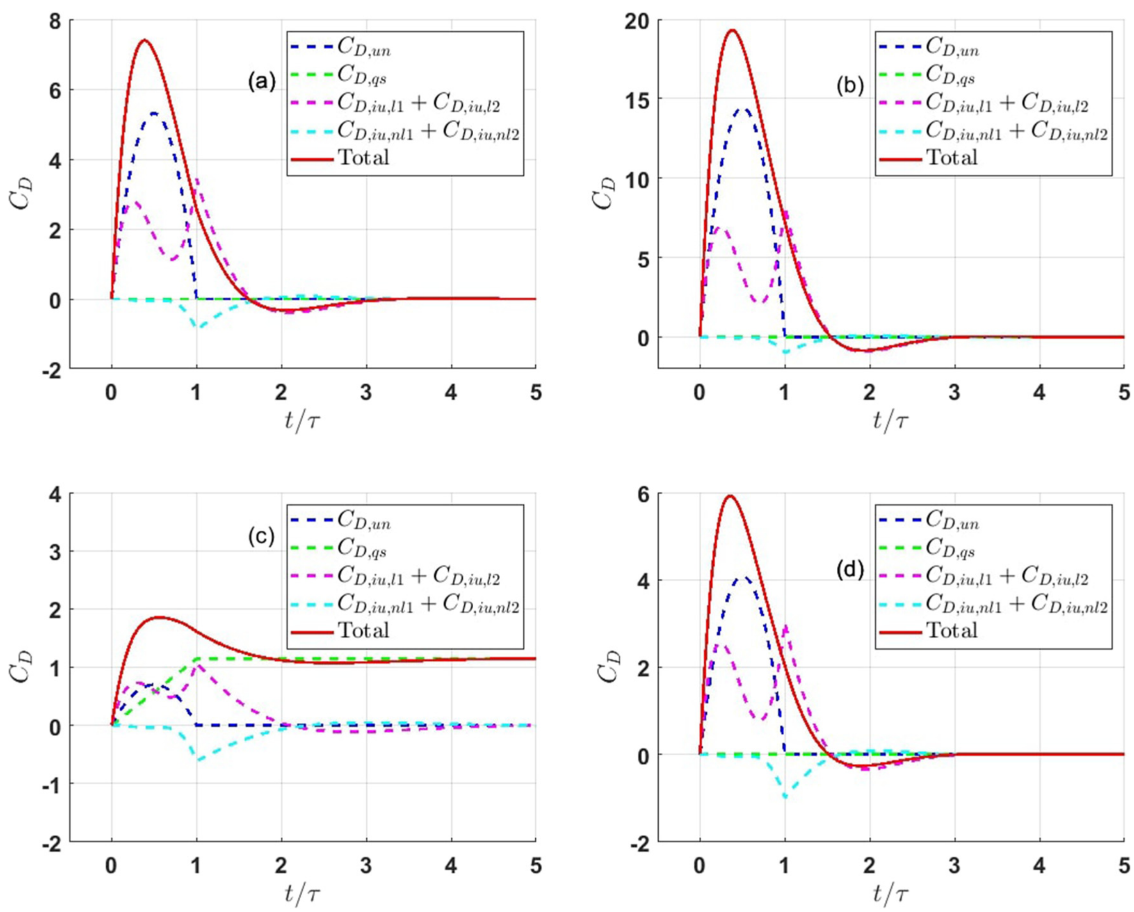

FIG. 8. Plot of each force component in C-MRG model on an isolated particle as a function of t/τ, $C_{D,un}$ (dashed blue), $C_{D,qs}$ (dashed green), $C_{D,iu,l1} + C_{D,iu,l2}$ (dashed magenta), $C_{D,iu,nl1} + C_{D,iu,nl2}$ (dashed cyan), total force (solid red), (a) air 1.22, (b) water 1.22, (c) air 3.0, and (d) water 3.0.

the shock and shows the characteristic oscillatory decay; (iii) the asymmetric nature of the total force about $t = \tau/2$ is amplified with the inclusion of compressibility effects, and as a result, the peak total force occurs noticeably before $t/\tau = 1/2$.

There have been past efforts where the force on a particle during shock particle interaction has been taken to be simply the sum of quasi-steady and undisturbed flow force contributions. This approximation is generally due to a lack of complete knowledge on the form of the inviscid unsteady force. From the figures, it is clear that such an approach, which ignores the inviscid unsteady contribution, does not capture the entire flow physics responsible for particle force. In particular, ignoring the inviscid unsteady contribution will underestimate peak force's magnitude and mispredict the time of the peak force. Also comparing the two figures shows the importance of the convolution integral to the drag model. The drag on a particle does not go to zero right after the shock moves downstream of the particle. Considering the past history of density-weighted relative acceleration in the C-MRG equation allows for the compressibility effects to be included in the prediction of the force.

A closer look will now be taken into the four parts that go into the inviscid unsteady force of the C-MRG model given in (18). In Fig. 9, the two linear and the two nonlinear contributions that makeup the inviscid unsteady force are shown for the Mach 1.22 case in water. From the figure, one can clearly see the linear terms to contribute a larger portion of the force than the nonlinear terms. $C_{D,iu,l1}$ (the blue line) contributes positively when the shock is located over the particle, and it qualitatively resembles the parabolic shape of the incompressible model. This force remains positive immediately after the shock passage and continues to undergo oscillatory decay. In contrast, $C_{D,iu,l2}$ (the green line) shows the largest variation throughout the shock-particle interaction. It quickly reaches a positive peak, then becomes negative to a minimum value of -6.5, and then reaches a second peak value of about 2 at $t = \tau$. Once the shock passes the particle, this component also undergoes oscillatory decay. It is clear that the dramatic change in the linear contribution from the incompressible to the compressible MRG model is due to the addition of $C_{D,iu,l2}$, which is absent in (2). The two nonlinear terms, $C_{D,iu,nl1}$ and $C_{D,iu,nl2}$, are somewhat different while the shock is over the particle, but after the shock has passed, these terms are almost identical.

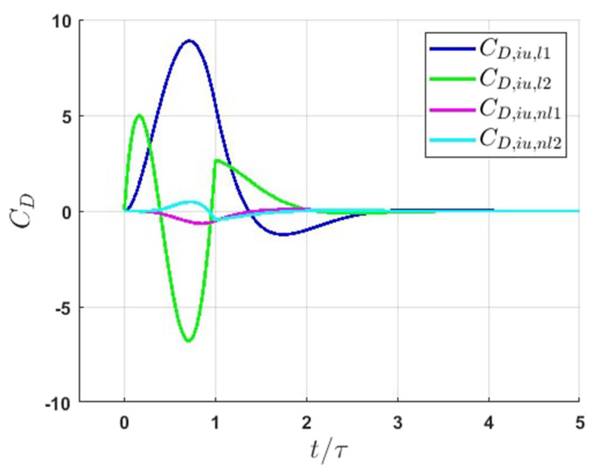

FIG. 9. Plot of each component of inviscid unsteady force for water 1.22 case, $C_{D,iu,l1}$ (blue), $C_{D,iu,l2}$ (green), $C_{D,iu,nl1}$ (magenta), and $C_{D,iu,nl2}$ (cyan).

B. Comparison with particle-resolved simulations

In this section, we compare the results of the particle-resolved simulations with the predictions of the following models: (i) incompressible MRG, (ii) compressible MRG with the zero-Mach kernel, and (iii) compressible MRG with the variable-Mach kernel. For air shock at $M = 1.22$, a further comparison is made with available experimental results. However, the experiments include viscous quasi-steady and unsteady contributions, which are ignored in the inviscid models. The comparison of the different drag coefficients is shown in Fig. 10 for all four cases considered. The incompressible MRG model always substantially overpredicts the peak drag force. By construction, it is symmetric about the time when the shock is over the center of the particle and does not capture the nonzero drag force after the shock has moved past the particle. The compressible MRG models capture the initial rise, peak drag magnitude, and peak drag time exceptionally well.

Though the agreement between the particle-resolved simulation results and those of C-MRG models is quite good, the model systematically underpredicts the force, during the decay phase after the shock has moved past the particle. The underprediction is small in the case of $M_s = 1.22$ water but is larger in the $M_s = 1.22$ air and $M_s = 3$ water cases. In both these cases, the post-shock Mach number is higher at 0.312 and 0.322, respectively. In the case of air at Mach 3, the C-MRG initially under-predicts, followed by over-prediction and then under-prediction. Unlike the other cases, there is substantial quantitative difference. There are two important reasons why the prediction is weaker in this cases. First, the Mach number of post-shock flow is supersonic. Thus, as the shock propagates over the particle, the Mach number of the flow changes from the initial zero value to greater than one. Even though the effect of this variable Mach number is expected to be strong, currently there does not exist a variable Mach number kernel that extends to the supersonic regime. In addition, the post-shock flow is characterized by the formation of a bow shock, whose presence is not accounted for in the models. These two effects must be accounted for with an improved kernel in order to achieve better prediction. The underprediction of the particle-resolved inviscid force (red curve) by the C-MRG constant kernel model (black curve) can be expected to be related to the finite Mach number of the post-shock flow. In particular, the use of the zero-Mach number kernel (8) results in a faster decay. The variable-Mach kernel slightly improves the model as expected based on the findings of Ref. 44, where they obtained K_{iu} for a range of Mach numbers and showed the kernel decay to slow down with increasing Mach number. For the Mach 3.0 air case, the post-shock Mach number was larger than 0.6, and the variable Mach kernel K_{iu} at such Mach number is unavailable. The difference between the simulation results and the C-MRG model indicates that the nonlinear effects are still not precisely captured by the variable-Mach kernel. This is due to the fact that the kernels were derived for a uniform flow. Therefore, one may need to develop modified kernels for application to the shock-particle interaction problem.

A comparison between drag calculated by C-MRG variable Mach kernel (solid green), PR simulation drag (solid red), and experimental results (solid blue) is shown in Fig. 11. The experimental data are taken from Ref. 12. Sun *et al.* measured the drag using an accelerometer in a

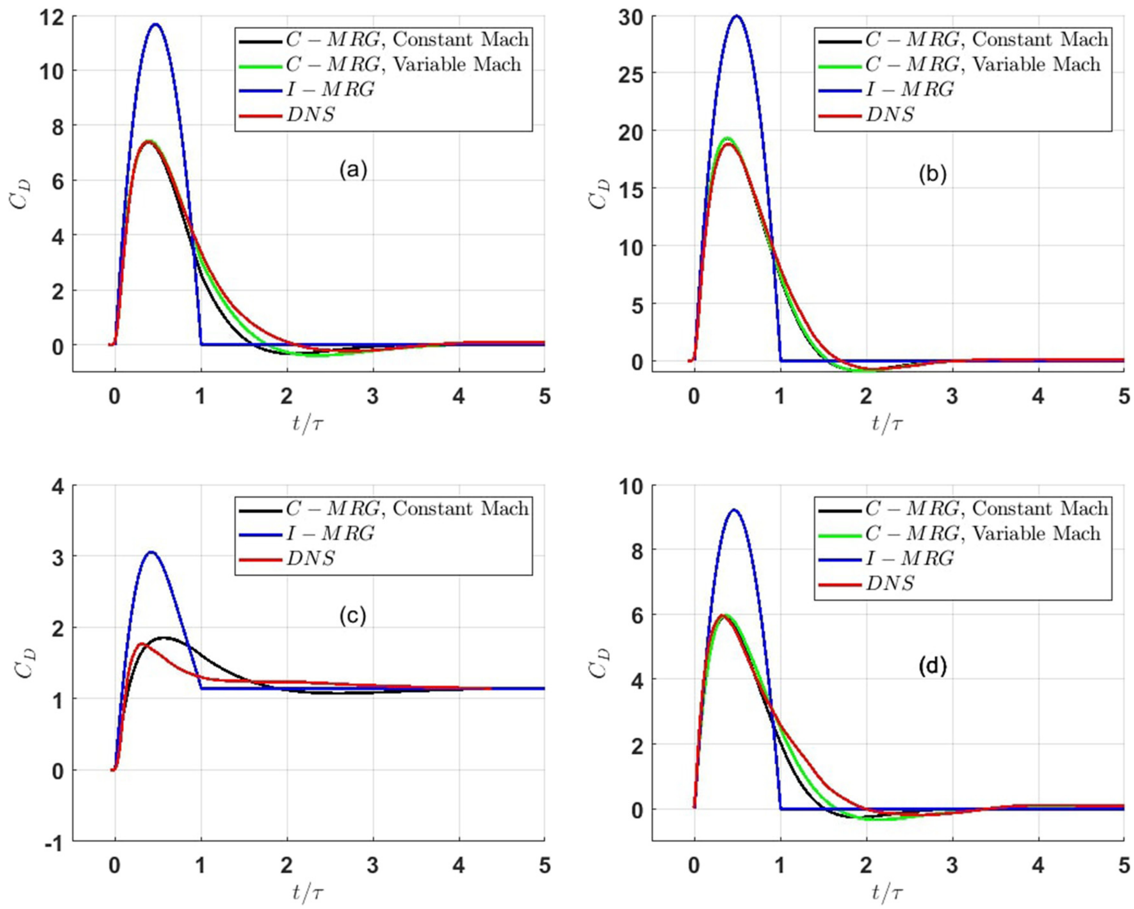

FIG. 10. Plot of each force component in the C-MRG model on an isolated particle as a function of t/τ, C-MRG constant Mach kernel (solid black), C-MRG variable Mach kernel (solid green), I-MRG (solid blue), and PR simulation (solid red), (a) air 1.22, (b) water 1.22, (c) air 3.0, and (d) water 3.0.

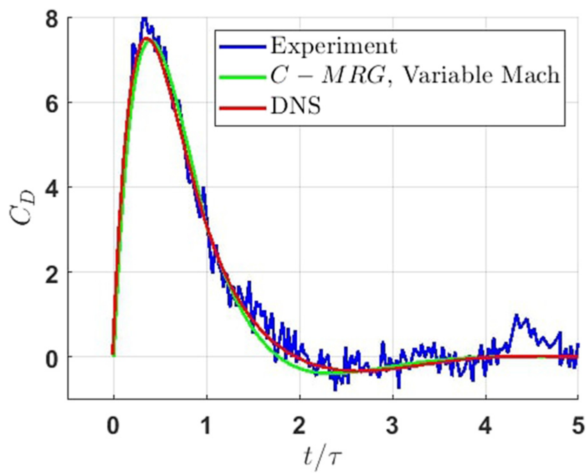

FIG. 11. Plot of C_D as a function of t/τ comparing C-MRG variable Kernel (solid green), PR simulation (solid red), and experimental data (solid blue).

vertical test tube using an 80 mm sphere with an incident shock Mach number of 1.22. The three lines show excellent agreement between the rise to the peak, the peak drag value, and the drag decay to zero. The small difference in the experimental data is caused by real-life factors that the simulation and force model do not consider, including viscosity.

While there are differences among the MRG model predictions and their approximation of the actual inviscid force, it is important to study how significant these differences are in the particle's long-term motion, which depends on the net impulse imparted to the particle. The impulse to the particle is the area under the drag force curve. In nondimensional terms, it is given by

$$I(t) = \int_{-\infty}^{t} C_D(t')\, dt', \tag{25}$$

where integration starts when the shock first touches the particle, which is also the moment when the particle force becomes nonzero. The four cases' impulse results are shown in Fig. 12. Plotted in the

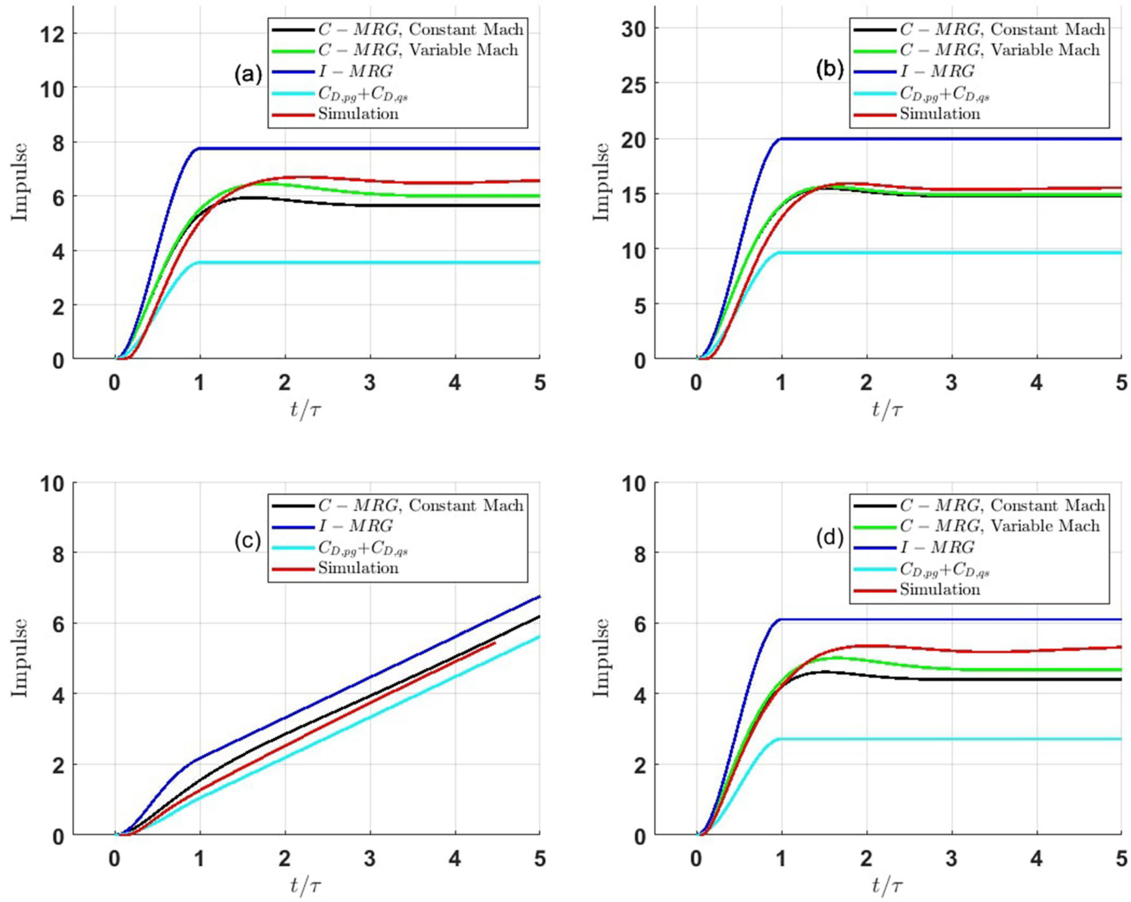

FIG. 12. Plot of impulse from C-MRG constant Mach kernel (solid black), C-MRG variable Mach kernel (solid green), I-MRG (solid blue), and $C_{D,un} + C_{D,qs}$ (solid cyan) models as a function of t/τ, (a) air 1.22, (b) water 1.22, (c) air 3.0, and (d) water 3.0.

figure are five curves corresponding to the C-MRG with the zero-Mach kernel in black, C-MRG with the variable-Mach kernel in green, I-MRG zero-Mach kernel in blue, the undisturbed flow plus quasi-steady force in cyan, and the simulation results as a red line. From the drag curves, it is known that the I-MRG impulse will be the same for $t > \tau$, except when the quasi-steady force is nonzero. However, in the C-MRG models, the impulse is expected to show an oscillatory convergence to the terminal value. The difference in impulse is clear from the figures. The I-MRG impulse is about 25% higher than the C-MRG impulses in all the cases. In the Mach 3.0 air case, the I-MRG is still 25% higher, but this is hard to see because of the nonzero quasi-steady inviscid force. There is only a slight difference in impulse between the zero-Mach and variable-Mach C-MRG models. The figures also show the total impulse computed only with the undisturbed flow force plus the inviscid quasi-steady force. This approximation has been used to compute particle force in incompressible and compressible flows. From the figures, one can see that the undisturbed flow and quasi-steady force substantially underestimate the total impulse. Thus, ignoring the inviscid unsteady force leads to a substantial underprediction of the net impulse.

VI. MODEL IMPLEMENTATION IN AN EULER–LAGRANGE SIMULATION

The force models described in Sec. II are now considered in the context of an Euler–Lagrange (EL) simulation of shock-particle interaction. Unlike the particle-resolved simulation, the flow around the particle will not be resolved in an EL simulation, and the force on the particle must be modeled. We will investigate how well the undisturbed and inviscid unsteady forces that are numerically computed with implementations of the different models compare with the analytical force calculated for an ideal shock of an infinitesimal thickness. (We will take the C-MRG model as the correct analytical force.) So the interest is twofold: (i) identity the grid resolution needed in an EL simulation to carry out the surface and volume averages of the C-MRG formulation and (ii) investigate the lack of convergence of the BBO models. Here, we point out that while the BBO models were not suitable in the analytical calculation of shock-induced force in Sec. III, the BBO models are easily implemented in the present EL simulations due to the finite thickness of the simulated shock.

The evaluation of the numerical implementations will be tested for the case of $M = 1.22$ air shock. The convergence behavior to be described is similar in all other cases and, therefore, will not be discussed. The key parameter of the EL problem is η, given by

$$\eta = \frac{d_p}{\Delta x}, \tag{26}$$

where d_p is the particle diameter and Δx is the grid cell-spacing. We will separately investigate the small particle ($\eta < 1$) and the large particle ($\eta > 1$) regimes. In the small particle regime, when $\eta \ll 1$, the particle surface and volume averages of flow properties approach the particle center values, leading to the BBO and MRG formulations being identically the same. On the other hand, when $\eta > 1$, the particle diameter is larger than the grid cell-spacing, the MRG model applicable since the surface and volume averages can be better approximated.

As mentioned in Sec. II A, the standard particle force model used in EL simulations is the I-BBO model, which relies on the instantaneous flow at the particle center to predict the force. In the more complex C-MRG formulation, the force depends on time-integrated surface and volume averages of the flow and, thus, represents a significant extension to the standard point-particle model. It must be stressed that the $\eta \gg 1$ results must be carefully interpreted. Clearly, in a simulation where the grid size is much smaller than the particle diameter, one could perform a fully resolved simulation. The purpose here is to demonstrate that if the undisturbed compressible flow variation on the scale of d_p is known then the force on a particle placed in such a flow can be predicted accurately with the C-MRG force expression.

In the following, we will briefly mention the surface and volume averages used in the EL simulation when the particle diameter is bigger than the grid spacing. Implementing the particle force models in the EL hydrocode is not the focus of this work, so only a brief description is given here. The surface and volume averaging techniques used in this work were inspired by the particle discretization methodology presented in Refs. 42 and 52. A computational particle is discretized using a nearly uniform distribution of marker points defined on the surface and throughout the particle's volume. The undisturbed flow properties are evaluated at these marker points, and then the particle surface or volume average is computed by averaging the requisite quantities over these points. The methodology implemented in this work displayed the same marker point density convergence behavior as.[52] The EL simulations in this work are one-way coupled, meaning that the fluid exerts a force on the particle, but the particle does not apply a force back to the fluid. Thus, the flow seen by the particle is indeed the undisturbed flow. In the limit when the particle is smaller than the grid spacing, for simplicity, we take the MRG formulation to be the same as the BBO formulation. However, more complex surface or volume averages can be calculated, but the difference is not substantial.

A. EL simulation results

First, we investigate the force on the particle when the grid size substantially smaller than the particle, so that surface and volume averages can be numerically calculated in the EL simulation. Figure 13 shows the comparison of pressure-gradient (undisturbed flow) force predictions of the I-BBO and C-MRG model formulations given in (1) and (5). Also the analytical pressure-gradient force computed as (13) is shown in the figures. The corresponding inviscid unsteady forces of I-BBO and C-MRG are shown in Fig. 14, where the analytical result is given in (18). From the results, it is apparent that the I-BBO formulation of pressure-gradient force does not converge—with increasing η the force magnitude continues to increase due to the sharp pressure jump of the shock front being better resolved, but the duration of pressure-gradient force correspondingly decreases to only when the shock is located near the particle center. The C-MRG formulation approaches the analytical limit for increasing η, and in particular, $\eta = 40$ provides an adequate approximation.

We now investigate the numerical implementation of the force models in the limit when the particle is comparable or smaller than the grid spacing. Typically, this is the limit in which most EL simulations are operated. In this limit, we only investigate the I-BBO and C-BBO models with their difference being in the latter the inviscid unsteady force is evaluated as a convolution integral in time. In this limit, since the flow is not resolved on the scale of the particle, surface and volume averages are the same as those evaluated at the particle center and, therefore, the MRG force expressions reduce to their BBO

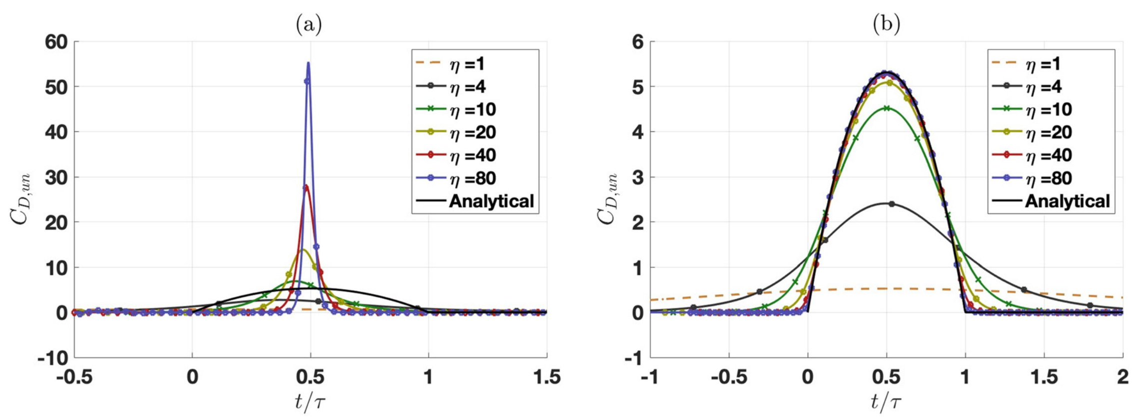

FIG. 13. Undisturbed (pressure-gradient) force prediction for a shock moving over a stationary isolated particle in an EL simulation of Mach 1.22 shock in air (i.e., A-LM configuration of Table II). Simulation results are plotted and labeled by their defining η value, with (a) I-BBO and (b) C-MRG theory.

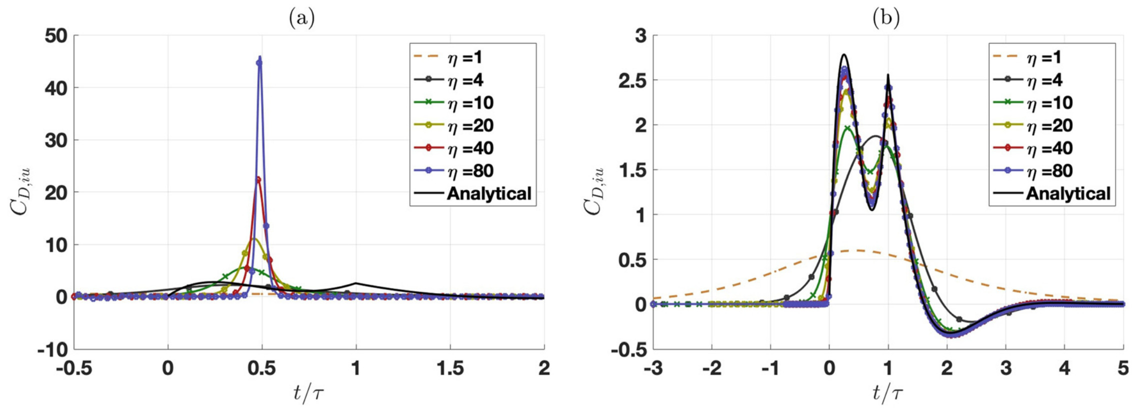

FIG. 14. Inviscid-unsteady force prediction for a shock moving over a stationary isolated particle in an EL simulation of Mach 1.22 shock in air (i.e., A-LM configuration of Table II). Simulation results are plotted and labeled by their defining η value, with (a) I-BBO and (b) C-MRG theory.

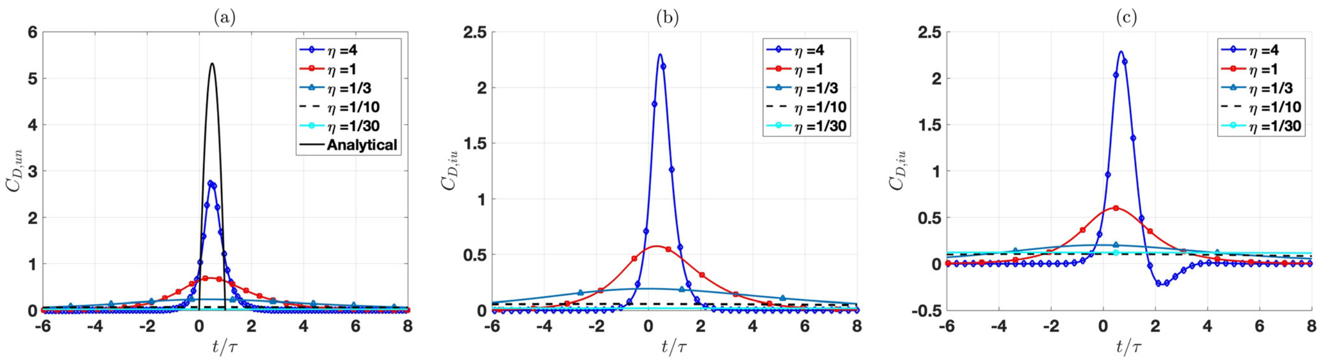

FIG. 15. EL simulation BBO force predictions for particles with $\eta \leq 4$, (a) undisturbed force, (b) inviscid-unsteady I-BBO force, and (c) inviscid-unsteady C-BBO force.

counterpart. However, both these forces are evaluated with the density-weighted fluid acceleration evaluated at the particle center. Figure 15(a) shows the time history of pressure-gradient force for varying values of η, which remains the same for I-BBO and C-BBO. Again the analytical pressure-gradient force given in (13) is shown. Contrary to the behavior seen for $\eta \gg 1$, when the particle size is much smaller than the grid, the pressure gradient is significantly weaker, leading to a much lower magnitude of the force. This force lasts for a much longer time and is not limited to only the period when the real shock is crossing the particle. Figures 15(b) and 15(c) show inviscid unsteady force calculated with numerical implementations of (1) and (3). Again we see the behavior that with decreasing particle size compared to the grid size, the force magnitude decreases, and the duration of force increases.

A numerical challenge arises in implementing C-BBO for $\eta < 1/3$. The EL simulation time step was determined by the Courant–Friedrichs–Lewy (CFL) stability condition for converged shock calculation. At smaller values of η, the time step needed for an accurate evaluation of the convolution integral becomes smaller than that required for CFL criterion. Table III displays the divergence of the total impulse for $\eta < 1/3$ in such cases. This is a situation to be avoided since even with a small enough time step the inviscid unsteady force computed with the C-BBO equation will lack the accuracy of a C-MRG simulation of similar computational expense. To avoid the computational burden, one might consider the I-BBO model. The difference between the I-BBO and C-BBO model predictions is small, with the main difference lying in the time history of the force predictions [see η >1 results in Figs. 15(b) and 15(c)]. While the I-BBO

TABLE III. EL simulation nondimensional particle force impulses, $I(\infty)$, for varying η are shown.

η	BBO F_{un}	MRG F_{un}	I-BBO F_{iu}	C-BBO F_{iu}	C-MRG F_{iu}
1/30	2.57		2.20	14.39	
1/10	2.58		2.20	4.16	
1/3	2.58		2.20	2.36	
1	2.58	2.15	2.20	2.22	2.38
4	2.58	2.83	2.20	2.20	2.37
10	2.58	3.57	2.20	2.20	2.10
20	2.58	3.55	2.20	2.20	2.10
40	2.58	3.54	2.20	2.20	2.10
80	2.60	3.55	2.20	2.20	2.09
Analytical	3.54	3.54	2.13	2.13	2.13

model results in a monotonic decay of inviscid unsteady force following the peak value, the kernel of the C-BBO model contributes to a nonmonotonic decay following the peak value. The total impulse for the C-BBO model is shown in Table III for several values of η. It is demonstrated that the C-BBO total impulse prediction converges to that of the I-BBO model when adequate temporal resolution is available for the evaluation of the convolution integral. For $1/3 < \eta < 1$, there is only very minor difference in time-history between I-BBO and C-BBO, and the total impulse follows this behavior. For cases of $\eta < 1/3$, the evaluation of the C-BBO convolution integral with adequate temporal resolution would be an expensive procedure with negligible advantage. Thus, it appears that if the particle in an EL simulation will be much smaller than the grid size, then it is appropriate to use the I-BBO approach and avoid the more stringent time step requirement of the convolution integral.

It is clear from the above discussion that it is not feasible to accurately capture the true time evolution of the pressure gradient and the inviscid unsteady forces when the particle is much smaller than the grid size—this is the penalty to be paid for inadequate resolution. It is then of interest to see if the time-integrated force or the net impulse on the particle is accurately computed by the models. The EL simulations' impulses are presented in Table III. The table shows a fascinating behavior that though the time history of forces shows great variation between different values of η, the net impulse remains nearly the same. This suggests that if one is not interested in time-accuracy, it is unnecessary to resolve the particle with a fine grid—the choice of the grid can be made independent of particle size. However, the undisturbed force of the BBO model is underpredicted by about 27%. This is due to the BBO formulation using the WENO-reconstructed pressure gradient at the particle center. The gradient reconstruction is required in the hydrocode to maintain stability as flow discontinuities propagate through the domain, but it somewhat smears the gradient at the particle location. This results in a loss of pressure-gradient impulse to the particle. This loss depends only on the gradient reconstruction methodology, and thus, once the error is established with a test problem whose exact solution is known (i.e., interaction with a planar shock), the error can be undone with a simple correction factor. For example, in the present code, the pressure-gradient force given by the first term on the right-hand side of (1) can be multiplied by a factor 1.37 to undo the gradient reconstruction error. In general, for EL simulations with particles much smaller than the grid size ($\eta \ll 1$), one cannot expect to determine a time-accurate force precisely because the time step will be larger than the time for the shock to traverse the particle. Hence, one can only realistically speak of conserving the impulse in these cases.

For simulations with $\eta > 1$, hydrodynamic information with increased spatial and temporal resolution becomes available for particle force computation. The C-MRG model can capture the analytical particle force behavior with ten grid points across the particle due to the force's accurate representation with a surface integration of pressure, which does not involve evaluation of spatial gradients across the shock. For the inviscid unsteady force, the EL implementation of the C-MRG model slightly underpredicts the analytical impulse, which displays a strong kink as the shock pass the trailing edge of the particle. Capturing this discontinuous force behavior perfectly in the EL simulation is challenging. The I-BBO model for all values of η overpredicts the inviscid unsteady force by about 3.3%, which is again due to numerical approximations in calculating the derivatives. Nevertheless, the error in impulse is quite small and, therefore, can be ignored.

VII. MODEL PERFORMANCE IN THE CASE OF A FREELY MOVING PARTICLE

So far we have evaluated the different models in the context of shock moving over a stationary particle. In this section, we demonstrate the applicability of these models for the case of freely moving particles as well. In particular, we will demonstrate the ability of the C-MRG model to accurately predict the time history of force even in the case of freely moving particles.

When considering the free motion of a particle in response to the force exerted on it by the shock, the density ratio between the particle and the post-shock fluid ($\rho = \rho_p/\rho_2$) comes as an additional important parameter. The stationary particle considered in Secs. IV, V, and VI can be considered as the infinite density ratio limit (i.e., as $\rho \to \infty$). When the density ratio is small, the particle will readily move as soon as the shock touches the upstream end. Due to the downstream particle motion, on the one hand, the shock (and the associated pressure jump) stays with the particle for a longer duration of time than in a stationary particle. On the other hand, with the particle motion, the relative velocity between the post-shock fluid and the particle decreases. It is of interest to see how well the C-MRG model is able to capture these complex competing effects.

Apart from the stationary case of $\rho \to \infty$, we studied two other density ratios of $\rho = 20$ and 2, for a Mach 1.22 shock in air. Particle-resolved simulations of these cases were performed in a coordinate system that is attached to the moving particle. The drag coefficient for these cases is shown in Fig. 16 as PR-$\rho = \infty$, PR-$\rho = 20$, and PR-$\rho = 2$. From the figure, it is clear that the density ratio 20 is large enough that its time history of force is almost the same as that of a stationary particle. It can also be seen that the PR simulation of density ratio 2 yields a lower C_D, which indicates a lower net force being imparted on the moving particle due to the shock.

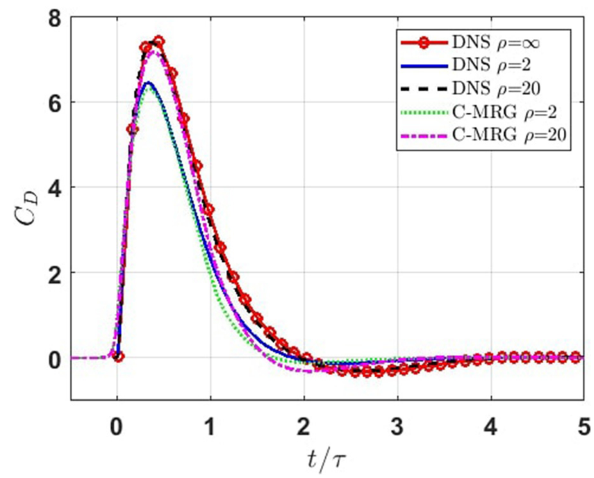

FIG. 16. Comparing force between moving particle and stationary particle simulations as a function of t/τ, PR simulation (red line with circles), PR simulation $\rho = 2$ (solid blue line), PR simulation $\rho = 20$ (dashed black line), C-MRG model $\rho = 2$ (dotted green line), and C-MRG model $\rho = 20$ (dot-dash magenta line).

Also shown in Fig. 16 is the C_D predicted by the C-MRG model for $\rho = 20$ and 2. In the case of a moving particle, both the velocity and the acceleration of the particle influence the force model. In the case of quasi-steady force, $\boldsymbol{F}_{qs}$ must be correctly based on the relative velocity between the fluid velocity averaged over the surface of the particle (which must account for the particle motion) and the particle velocity. In the present inviscid investigation, the quasi-steady force is identically zero for the low Mach number shock. The inviscid unsteady force must account for the time rate of change in particle motion and the inviscid unsteady force given in Eq. (5) must be modified as

$$\boldsymbol{F}_{iu} = \underbrace{3V_p \int_{-\infty}^{t} K_{iu} \left[\frac{d\overline{(\rho^g u^g_{r,x})}^S}{dt} - \frac{d\overline{(\rho^g u^P_{r,x})}^S}{dt} + \overline{\rho^g (\boldsymbol{u}^g \boldsymbol{u}^P)}^V \cdot \nabla (\overline{u^g_{r,x}}^S) \right]_{\xi} d\xi}_{\boldsymbol{F}_{iu} = \boldsymbol{F}_{iu,l} + \boldsymbol{F}_{iu,nl} + \boldsymbol{F}_{iu,p}}, \tag{27}$$

where the superscripts g and P represent the fluid and particle properties, respectively. In the above, the inviscid unsteady force has three contributions—apart from the linear and nonlinear contributions, the second term on the right-hand side is a third contribution due to particle motion. The definition of undisturbed flow force remains the same. The sum of the undisturbed flow force and the inviscid unsteady force is used to calculate the total C_D predicted by the C-MRG model, which are shown in Fig. 16. For the $\rho = 20$ particle, the agreement between the C-MRG model and the PR simulation results is similar to those of the stationary particle, due to the very slow motion of the particle. It is clear that the C-MRG model is quite accurate in capturing the magnitude and timing of the peak force even in the case of a moving particles, which are substantially different from those of the stationary particle. It can be noted that as a result of particle motion, the negative loop of C_D is substantially reduced. The slight under-prediction of the force at intermediate times by the C-MRG model still persists.

The results of $\rho = 2$ case can be broken down into separate components to determine what causes the deviation from the stationary particle case. Shown in Fig. 17(a) is the breakdown of forces into the undisturbed flow force and the inviscid unsteady force for both the $\rho \to \infty$ and $\rho = 2$ cases. The dotted green and solid blue lines represent the undisturbed force, which is approximately the same between the stationary and moving particle cases. Also the undisturbed flow force remains nonzero for a slightly longer time for the moving particle. On the whole, the effect of the particle moving with the shock, and as a result experiencing the jump in pressure for a longer duration of time, is not significant. However, the inviscid unsteady force shown as dashed green and dotted blue lines in Fig. 17(a) shows significant difference between the two cases. The three components of the inviscid unsteady force, given in (27), are shown in Fig. 17(b) along with the stationary inviscid unsteady force. The linear portion on the force, represented by the solid black and dashed green lines, is approximately the same. The second sharp peak is not as distinct in the moving particle case. Additionally, the nonlinear force contribution is close although a systematic reduction in both the linear and nonlinear contributions result due to particle motion. The cause for the noticeable difference in the inviscid unsteady force is due to the additional term that arises from particle motion. The magenta line with circles shown in Fig. 17(b) corresponds to the portion of the inviscid unsteady kernel that accounts for the particle movement.

The other important variables in a moving particle simulation are the velocity and the position of the particle. Shown in Fig. 18 are plots showing the velocity and particle position for the different cases. The solid blue line represents PR simulation of $\rho = 2$, and it is in great agreement with the dotted green line of the corresponding C-MRG prediction. The velocity and particle position for $\rho = 2$ case are much greater than those of $\rho = 20$ PR simulation represented by the dashed black line and the C-MRG model shown by the dot-dash magenta line. In Fig. 18(a), the particle velocity is scaled by the speed of sound in the ambient air. It is seen that the velocity for the density ratio 2 case reaches a maximum value of about 18% of ambient speed of sound then stays constant after the shock has passed. As expected, for the $\rho = 20$ case, the peak value is a small value of 2.5% the ambient speed of sound. Additionally, when looking at the particle movement scaled by the particle diameter in Fig. 18(b), the density ratio 20 case has not significantly moved during interaction with the shock, thus explaining the closeness of the C_D plots with that of a stationary

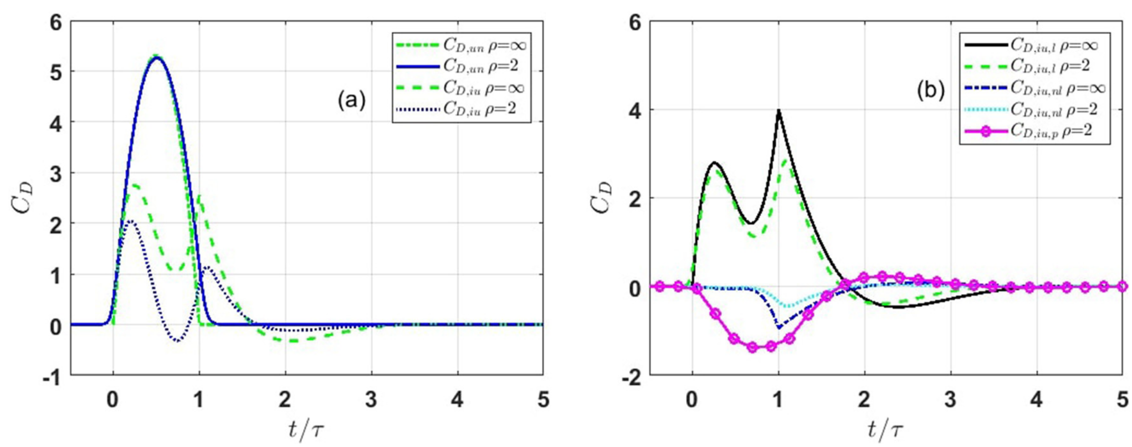

FIG. 17. Comparing force components between the moving and stationary particle simulations as a function of t/τ, (a) $C_{D,un}$ (dot-dash green line), $C_{D,un}$ $\rho = 2$ (solid blue line), $C_{D,iu}$ (dashed green line), and $C_{D,iu}$ $\rho = 2$ (dotted blue line). (b) Breakdown of inviscid unsteady force moving particle vs stationary particle $C_{D,iu,l}$ (solid black line), $C_{D,iu,l}$ $\rho = 2$ (dot dash blue line), $C_{D,iu,nl}$ (dashed green line), $C_{D,iu,nl}$ $\rho = 2$ (dotted cyan line), $C_{D,iu,P}$ $\rho = 2$ (magenta line with circles).

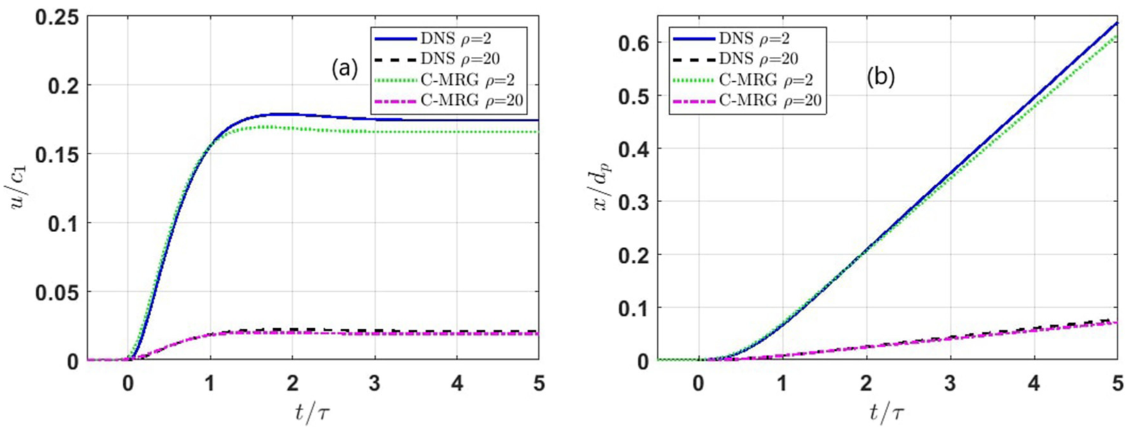

FIG. 18. Comparing particle velocity (a) and position (b) for the PR simulation $\rho = 2$ (solid blue line), PR simulation $\rho = 20$ (dashed black line), C-MRG model rho = 2 (dotted green line), C-MRG model $\rho = 20$ (dotted green line), and as a function of t/τ.

particle. Even the $\rho = 2$ particle has moved by less than $0.1d_p$ over one shock interaction time.

VIII. CONCLUSION

This paper investigates modeling the drag force experienced by an isolated particle when interacting with an incident shock wave. Particle-resolved simulations were carried out at two different shock Mach numbers for water and air as the fluid medium. These results were then compared to four different force prediction models that progressively included more physics. These models focus only on the inviscid mechanisms that occur at early times of shock-particle interaction and aim to capture the particle's inviscid drag. The four models considered are (i) incompressible BBO model, which ignored the compressibility effects as well as the finite particle size compared to shock thickness, (ii) compressible BBO, which only overlooks the finite particle size, (iii) incompressible MRG, which ignores the compressibility effects, and finally (iv) compressible BBO model, which is the most accurate. Immediately following the interaction with the shock, the drag rapidly increases reaches a peak, whose magnitude and time of occurrence are well predicted by C-MRG model. The simulation results and C-MRG model prediction are almost identical at lower shock Mach numbers. In comparison, at higher Mach numbers, nonlinear effects become important, and the late time decay is slightly different between the simulation results and the model prediction. The force prediction model performs well both for air as the fluid medium, modeled with an ideal gas equation of state and for water, modeled with a stiffened gas equation of state. The results also clearly reveal the vital fact that the drag coefficient for shock-particle interaction is strongly dependent on the equation of state, so that C_D for one medium cannot be used for the other. One must apply the force model with the appropriate unsteady contribution to accurately capture the force's time evolution. One of the major reasons to use these models for predicting particle force is that it is EOS independent. The only inputs in the model are the fluid properties on both sides of the shock.

The paper also investigates the implementation of the different force models in a one-way coupled Euler–Lagrangian simulation of shock particle interaction, where the flow around the particle is not resolved. In MRG models, the surface and volume averages of the undisturbed fluid quantities are obtained by distributing surface and volume marker points and appropriately integrating the interpolated values. In the EL simulations, the parameter $\eta = d_p/\Delta x$ representing the number of grid points per particle diameter was varied over a wide range. For $\eta > 10$, we observe that the numerical implementation of the C-MRG model captures the particle's force in a time-accurate manner. The other models cannot recover the time variation of particle force accurately even with a number of grid points resolving the particle. The more appropriate regime of interest to EL simulations is when $\eta \ll 1$. In this limit, surface and volume averages are not possible since the particle is much smaller than the grid and the recommended force modeling approach is I-BBO. Although the time history of force calculated with this model will not be accurate, the quest is to compute the particle's net impulse. We observe that the I-BBO model recovers the inviscid unsteady force's impulse accurately. The impulse of the pressure gradient is underpredicted due to the dissipative nature of WENO-reconstruction of pressure gradient at the particle center. One possible remedy is to apply a correction factor of 1.37 to undo the gradient reconstruction error. Nevertheless, it must be cautioned that matching the impulse may be sufficient for a nearly stationary particle. In the case of particles undergoing substantial motion due to the initial inviscid force, the time history of force becomes essential, and the net impulse depends on the particle motion. This requires further detailed investigation.

When considering the movement of a particle, the density ratio between the particle and the fluid plays a key role. It was shown that for a case where $\rho = 20$, the C-MRG model for a stationary particle produces almost identical results to a PR simulation. When the value of ρ is smaller, the difference in drag from the stationary case can be attributed to the additional term in the inviscid unsteady force that accounts for particle acceleration.

ACKNOWLEDGMENTS

This work was supported by the Office of Naval Research under the Naval Undersea Research Program (NURP), Contract No. N000141812478. This work was also partly supported in part by the U.S. Department of Energy, National Nuclear Security

Administration, Advanced Simulation and Computing Program, as a Cooperative Agreement under the Predictive Science Academic Alliance Program, under Contract No. DE-NA0002378.

AUTHOR DECLARATIONS

Conflict of Interest

The authors have no conflicts to disclose.

DATA AVAILABILITY

The data that support the findings of this study are available from the corresponding author upon reasonable request.

APPENDIX: SURFACE AND VOLUME INTEGRATION IDENTITIES

Consider a sharp planar front, such as a shock, located at a nondimensional distance $\tilde{x}_s(\tilde{t})$ from the origin as shown in Fig. 2. Let fluid properties abruptly change across the discontinuity. For example, the fluid property f to the right (or ahead) of the front is f_1, while it is f_2 to the left (or behind) the front. We now define volume and surface-averaged fields as

$$\bar{f}^V(x,t) = \frac{1}{V}\oint_V f(\boldsymbol{x}', t)\, d\boldsymbol{x}' \quad \text{and} \quad \bar{f}^S(x,t) = \frac{1}{S}\oint_S f(\boldsymbol{x}', t)\, d\boldsymbol{x}', \quad \text{(A1)}$$

where the volume and surface averages are over a sphere of unit radius centered around the origin. Due to the 1D nature of the sharp planar front, the resulting volume or surface average is also 1D. When the averaging sphere is fully to one side of the sharp planar front, the averaging process simply yields the local uniform value. Provided $-1 \le \tilde{x}_s \le 1$ the sharp front intersects the particle. In this limit, when the front is located within the particle, the following two identities for the volume and surface averages of the fluid property can be obtained:

$$\bar{f}^V = \frac{3}{4}\left(\tilde{x}_s - \frac{1}{3}\tilde{x}_s^3\right)(f_2 - f_1) + \frac{1}{2}(f_1 + f_2), \quad \text{(A2)}$$

$$\bar{f}^S = \frac{\tilde{x}_s}{2}(f_2 - f_1) + \frac{1}{2}(f_1 + f_2). \quad \text{(A3)}$$

The above identities can be readily proven by noting that the nondimensional volume of the spherical cap of the particle that is immersed in f_1 is $\pi(1-\tilde{x}_s)^2(2+\tilde{x}_s)/3$ and the corresponding nondimensional surface area of the spherical cap is $2\pi(1-\tilde{x}_s)$.

The time and x derivatives of the volume and surface averages can be obtained by making the substitution $\tilde{x}_s = \tilde{\xi}_s(\tilde{t}) - \tilde{x}$, then taking the derivative, and setting $\tilde{x} = 0$ for a stationary particle located at the origin to obtain the following identities:

$$\frac{\partial}{\partial t}\bar{f}^S = \frac{c_2}{R_p}\frac{M_s}{2}(f_2 - f_1), \quad \text{(A4)}$$

$$\frac{\partial}{\partial t}\bar{f}^V = \frac{c_2}{R_p}\frac{3}{4}M_s\left(1 - \tilde{x}_s^2\right)(f_2 - f_1), \quad \text{(A5)}$$

$$\frac{\partial}{\partial x}\bar{f}^V = -\frac{1}{R_p}\frac{3}{4}\left(1 - \tilde{x}_s^2\right)(f_2 - f_1). \quad \text{(A6)}$$

The derivation of the above identities makes use of the definition that the shock Mach number is the nondimensional speed of the shock. Also the particle is taken to be stationary at the origin. Similarly, we can also prove the following two identities:

$$\frac{\partial}{\partial t}\overline{\left(x'\frac{\partial f}{\partial x'}\right)}^V = \frac{c_2}{R_p}\frac{3}{4}M_s\left(3\tilde{x}_s^2 - 1\right)(f_2 - f_1), \quad \text{(A7)}$$

$$\frac{\partial}{\partial x}\overline{\left(x'\frac{\partial f}{\partial x'}\right)}^V = -\frac{1}{R_p}\frac{3}{4}\left(3\tilde{x}_s^2 - 1\right)(f_2 - f_1). \quad \text{(A8)}$$

These identities can be derived by letting $\partial f/\partial \tilde{x}' = (f_1 - f_2)\,\delta(\tilde{x}' - \tilde{\xi}_s)$ and performing integral of the generalized function.

REFERENCES

[1] A. W. Woods, "The fluid dynamics and thermodynamics of eruption columns," Bull. Volcanol. **50**(3), 169–193 (1988).

[2] Y. Liu and M. A. F. Kendall, "Numerical analysis of gas and micro-particle interactions in a hand-held shock-tube device," Biomed. Microdevices **8**(4), 341–351 (2006).

[3] Y. Mehta, T. L. Jackson, J. Zhang, and S. Balachandar, "Numerical investigation of shock interaction with one-dimensional transverse array of particles in air," J. Appl. Phys. **119**(10), 104901 (2016).

[4] C. Mao, T. Jin, K. Luo, and J. Fan, "Investigation of supersonic turbulent flows over a sphere by fully resolved direct numerical simulation," Phys. Fluids **31**(5), 056102 (2019).

[5] T. Saito, M. Saba, M. Sun, and K. Takayama, "The effect of an unsteady drag force on the structure of a non-equilibrium region behind a shock wave in a gas-particle mixture," Shock Waves **17**(4), 255–262 (2007).

[6] Z. Hosseinzadeh-Nik, S. Subramaniam, and J. D. Regele, "Investigation and quantification of flow unsteadiness in shock-particle cloud interaction," Int. J. Multiphase Flow **101**, 186–201 (2018).

[7] Y. Mehta, C. Neal, K. Salari, T. L. Jackson, S. Balachandar, and S. Thakur, "Propagation of a strong shock over a random bed of spherical particles," J. Fluid Mech. **839**, 157 (2018).

[8] Y. Mehta, K. Salari, T. L. Jackson, and S. Balachandar, "Effect of Mach number and volume fraction in air-shock interacting with a bed of randomly distributed spherical particles," Phys. Rev. Fluids **4**(1), 014303 (2019).

[9] P. Das, O. Sen, K. K. Choi, G. Jacobs, and H. S. Udaykumar, "Strategies for efficient machine learning of surrogate drag models from three-dimensional mesoscale computations of shocked particulate flows," Int. J. Multiphase Flow **108**, 51–68 (2018).

[10] A. N. Osnes, M. Vartdal, M. G. Omang, and B. A. P. Reif, "Computational analysis of shock-induced flow through stationary particle clouds," Int. J. Multiphase Flow **114**, 268–286 (2019).

[11] A. N. Osnes, M. Vartdal, M. G. Omang, and B. A. P. Reif, "Particle-resolved simulations of shock-induced flow through particle clouds at different Reynolds numbers," Phys. Rev. Fluids **5**(1), 014305 (2020).

[12] M. Sun, T. Saito, K. Takayama, and H. Tanno, "Unsteady drag on a sphere by shock wave loading," Shock Waves **14**(1), 3–9 (2005).

[13] B. W. Skews, M. S. Bredin, and M. Efune, "Drag measurement in unsteady compressible flow Part 2: Shock wave loading of spheres and cones," Shock **1**(1.2), 1–3 (2007).

[14] M. Parmar, A. Haselbacher, and S. Balachandar, "Modeling of the unsteady force for shock-particle interaction," Shock Waves **19**(4), 317–329 (2009).

[15] J. L. Wagner, S. J. Beresh, S. P. Kearney, B. O. Pruett, and E. K. Wright, "Shock tube investigation of quasi-steady drag in shock-particle interactions," Phys. Fluids **24**(12), 123301 (2012).

[16] Y. Ling, A. Haselbacher, and S. Balachandar, "Importance of unsteady contributions to force and heating for particles in compressible flows: Part 1: Modeling and analysis for shock-particle interaction," Int. J. Multiphase Flow **37**(9), 1026–1044 (2011).

[17] Y. Ling, A. Haselbacher, and S. Balachandar, "Importance of unsteady contributions to force and heating for particles in compressible flows. Part 2: Application to particle dispersal by blast waves," Int. J. Multiphase Flow **37**(9), 1013–1025 (2011).

[18] O. Igra and K. Takayama, "Shock tube study of the drag coefficient of a sphere in a non-stationary flow," Proc. R. Soc. London, Ser. A **442**(1915), 231–247 (1993).

[19] A. Britan, T. Elperin, O. Igra, and J. P. Jiang, "Acceleration of a sphere behind planar shock waves," Exp. Fluids **20**(2), 84–90 (1995).
[20] H. Tanno, T. Komuro, M. Takahashi, K. Takayama, H. Ojima, and S. Onaya, "Unsteady force measurement technique in shock tubes," Rev. Sci. Instrum. **75**(2), 532–536 (2004).
[21] H. Tanno, K. Itoh, T. Saito, A. Abe, and K. Takayama, "Interaction of a shock with a sphere suspended in a vertical shock tube," Shock Waves **13**(3), 191–200 (2003).
[22] E. Loth, "Compressibility and rarefaction effects on drag of a spherical particle," AIAA J. **46**(9), 2219–2228 (2008).
[23] Y. Ling, A. Haselbacher, and S. Balachandar, "Transient phenomena in one-dimensional compressible gas-particle flows," Shock Waves **19**(1), 67–81 (2009).
[24] Y. Ling, A. Haselbacher, S. Balachandar, F. M. Najjar, and D. S. Stewart, "Shock interaction with a deformable particle: Direct numerical simulation and point-particle modeling," J. Appl. Phys. **113**(1), 013504 (2013).
[25] J. A. K. Horwitz and A. Mani, "Accurate calculation of Stokes drag for point-particle tracking in two-way coupled flows," J. Comput. Phys. **318**, 85–109 (2016).
[26] P. J. Ireland and O. Desjardins, "Improving particle drag predictions in Euler-Lagrange simulations with two-way coupling," J. Comput. Phys. **338**, 405–430 (2017).
[27] S. Balachandar, K. Liu, and M. Lakhote, "Self-induced velocity correction for improved drag estimation in Euler-Lagrange point-particle simulations," J. Comput. Phys. **376**, 160–185 (2019).
[28] *Multiphase Flow Handbook*, edited by C. T. Crowe (CRC Press, 2005).
[29] M. Parmar, A. Haselbacher, and S. Balachandar, "Generalized Basset-Boussinesq-Oseen equation for unsteady forces on a sphere in a compressible flow," Phys. Rev. Lett. **106**(8), 084501 (2011).
[30] M. R. Maxey and J. J. Riley, "Equation of motion for a small rigid sphere in a nonuniform flow," Phys. Fluids **26**(4), 883–889 (1983).
[31] R. Gatignol, "The Faxen formulae for a rigid particle in an unsteady non-uniform Stokes flow," J. Mec. Theor. Appl. **2**, 143–160 (1983).
[32] M. Parmar, A. Haselbacher, and S. Balachandar, "Equation of motion for a sphere in non-uniform compressible flows," J. Fluid Mech. **699**, 352 (2012).
[33] S. Annamalai and S. Balachandar, "Faxén form of time-domain force on a sphere in unsteady spatially varying viscous compressible flows," J. Fluid Mech. **816**, 381 (2017).
[34] A. V. Fedorov, A. V. Shul'gin, and S. V. Poplavski, "Motion of a particle behind the shock wave front," Combust., Explos., Shock Waves **46**(2), 207–215 (2010).
[35] C. B. Henderson, "Drag coefficients of spheres in continuum and rarefied flows," AIAA J. **14**(6), 707–708 (1976).
[36] M. Parmar, A. Haselbacher, and S. Balachandar, "Improved drag correlation for spheres and application to shock-tube experiments," AIAA J. **48**(6), 1273–1276 (2010).
[37] E. Loth, "Quasi-steady shape and drag of deformable bubbles and drops," Int. J. Multiphase Flow **34**(6), 523–546 (2008).
[38] A. B. Basset, *A Treatise on Hydrodynamics: With Numerous Examples* (Bell and Company, Deighton, 1888), Vol. 2.
[39] J. Boussinesq, "On the resistance that an indefinite fluid opposes at rest, without gravity, to the movement varies from a solid sphere that it wets over its entire surface, when the speeds remain very continuous and low enough for their edges and products to be negligible," C. R. Acad. Sci. Paris **100**, 935–937 (1885).
[40] C. W. Oseen, *Newer Methods and Results in Hydrodynamics* (Akademische Verlagsgesellschaft mbH, Leipzig, 1927).
[41] G. I. Taylor, "The forces on a body placed in a curved or converging stream of fluid," Proc. R. Soc. London, Ser. A **120**(785), 260–283 (1928).
[42] S. Nili, C. Park, R. T. Haftka, N. H. Kim, and S. Balachandar, "Effect of finite particle size on convergence of point particle models in Euler-Lagrange multiphase dispersed flow," in *APS Division of Fluid Dynamics Meeting Abstracts* (APS, 2017), p. L2-005.
[43] A. L. Longhorn, "The unsteady, subsonic motion of a sphere in a compressible inviscid fluid," Q. J. Mech. Appl. Math. **5**(1), 64–81 (1952).
[44] M. Parmar, A. Haselbacher, and S. Balachandar, "On the unsteady inviscid force on cylinders and spheres in subcritical compressible flow," Philos. Trans. R. Soc. A **366**(1873), 2161–2175 (2008).
[45] R. B. Koneru and S. Balachandar, "An assessment of the drag models in the case of a shock interacting with a fixed bed of point particles," J. Fluids Eng. **143**(1), 011401 (2021).
[46] M. S. Liou, "A sequel to AUSM: AUSM$^+$," J. Comput. Phys. **129**(2), 364–382 (1996).
[47] A. Haselbacher, "A WENO reconstruction algorithm for unstructured grids based on explicit stencil construction," AIAA Paper No. 2005-879, 2005.
[48] Y. Ling, J. L. Wagner, S. J. Beresh, S. P. Kearney, and S. Balachandar, "Interaction of a planar shock wave with a dense particle curtain: Modeling and experiments," Phys. Fluids **24**(11), 113301 (2012).
[49] P. O. Persson and G. Strang, "A simple mesh generator in MATLAB," SIAM Rev. **46**(2), 329–345 (2004).
[50] H. Si, "TetGen, a Delaunay-based quality tetrahedral mesh generator," ACM Trans. Math. Software **41**(2), 1–36 (2015).
[51] Y. Mehta, C. Neal, T. L. Jackson, S. Balachandar, and S. Thakur, "Shock interaction with three-dimensional face centered cubic array of particles," Phys. Rev. Fluids **1**(5), 054202 (2016).
[52] M. Uhlmann, "An immersed boundary method with direct forcing for the simulation of particulate flows," J. Comput. Phys. **209**(2), 448–476 (2005).